

Loïc Broyer

**Nanotechnologies for the ICTs
2021**

EPFL – Microsystems 1 laboratory

Cryogenic thermometry based on superconducting microwave resonators

from 23/02/21 to 20/08/21

Confidentiality : no

Under the supervision of :

- **Company supervisor : Dr. Hernán FURCI (hernan.furci@epfl.ch)**
Present at the defense : yes
- **Phelma Tutor : Prof. Thierry OUISSE (thierry.ouisse@phelma.grenoble-inp.fr)**

**Ecole nationale
supérieure de physique,
électronique, matériaux**

Phelma
Bât. Grenoble INP - Minatec
3 Parvis Louis Néel - CS 50257
F-38016 Grenoble Cedex 01

Tél +33 (0)4 56 52 91 00
Fax +33 (0)4 56 52 91 03

<http://phelma.grenoble-inp.fr>

Figure 1: The Gantt chart of the project.

Dates	March		April		May		June		July		August	
Task												
Theoretical Analysis												
Writing the design code												
Clean Room training												
Fabrication method development												
Final sample production												
Thesis writing												
Cryogenic experiments												

Preface

This thesis, named "Cryogenic thermometry based on superconducting microwave resonators" was realized between March and August 2021 under the supervision of Dr. Hernán Furci and responsibility of Dr. Giovanni Boero. The tasks for the project were split between me and André Chatel, a newly starting PhD student.

This project took place in Prof. Jürgen Brugger's Microsystems Laboratory 1 (LMIS1) laboratory from EPFL. This laboratory has a wide experience in microfabrication and microsystems, which was valuable for this project. More specifically, one field of research investigated is the realization of micro NMR and ESR spectroscopy tools [1], [2]. The team involved in this field has an extensive experience in radiofrequency microresonators and cryogenic systems, which has led to fruitful discussions. They also possess a cryogenic RF station that can reach temperatures as low as 1.4 K and that was used for the measurements, essential for the characterization of the developed devices.

The fabrication of the samples took place in the CMi RD cleanroom from EPFL. This is a class 100 cleanroom with a variety of tools available for the fabrication of micro and nano-systems. An amount of 4000 CHF was granted by EPFL to conduct operations in CMi, in the frame of my Master thesis.

The direct costs related to the realisation of this thesis are represented by the microfabrication expenses. The materials and operation fees involved in this project reached a total of 4500 CHF.

A Gantt chart presenting the real time organization of the project can be found in fig. 1

Acknowledgements

I wish to thank all the people who provided support during the research and the writing of this thesis.

First, I am thankful to my thesis supervisor, Dr. Hernán Furci for providing guidance and technical support throughout the research process, as well as for his precious proof-reading of my report. I also wish to thank Dr. Giovanni Boero, who helped with insightful discussions and technological expertise with the cryostat system. Also, I thank Prof. Jürgen Brugger, who hosted me in his lab and Prof. Thierry Ouisse who will evaluate my thesis work.

I also want to thank the CMi for providing a 4000 CHF grant to be used in the cleanroom, as well as the CMi staff whose expertise was very useful for debugging machines and processes.

I am thankful to my colleagues in the LMIS1 lab with who I had technical - or not - discussions. Especially André Chatel with who I collaborated on this project, Roberto Russo who helped us with his knowledge about NbTi processing and Reza Farsi who helped with the PCB design and the wire-bonding of the chips.

Finally, I want to thank my parents and my family for supporting me throughout my studies, and especially my grandfather who inspired me to follow scientific studies.

Glossary

CPW	Coplanar Waveguide.	8
EDX	Electron Dispersive X-Ray analysis.	38
IBE	Ion Beam Etching.	33
MKID	Microwave Kinetic Inductance Detector.	8
NEP	Noise Equivalent Power.	16
SEM	Scanning Electron Microscope.	38

List of Figures

1	Gantt chart of the project	2
2	Sketch of a MKID layout	9
3	Illustration of the working principle of MKIDs, reproduced from [3]	10
4	Plot of the mean field type phase diagram for type I and type II superconductors. Reproduced from [4]	14
5	Plots of equations of the superconductivity theory.	15
6	Theoretical superconducting line impedance per unit of length.	17
7	Electrical model of a transmission line	20
8	Differential section of a transmission line	20
9	Cross sectional representation of a coplanar waveguide (without background ground plane). Dark blue represents the conductor surface region penetrated by the magnetic field (London depth).	21
10	Illustration of the waveguide modes.	22
11	Theoretical variation of the resonance frequency with temperature.	24
12	Example of a two-port signal flow graph.	25
13	COMSOL simulation of S parameters of CPW meandered resonators.	28
14	Process flows (Lift-off and etching) for the fabrication of CPW	30
15	Schematics of the resolution test structures used	31
16	Schematic of the pad test structures	31
17	Representation of the lift-off bi-layer resist structure after development.	33
18	IBE etched tapered gap.	35
19	IBE reflow comparison	36
20	IBE underdevelopment pattern	36
21	SPTS etched depth against time.	38
22	Fluoridated resist stripping	38
23	Comparison of lift off processes for two superconducting film thicknesses.	39
24	Comparison of the L resolution test structures.	40
25	Resolution test structures of the final plasma etched wafer.	40
26	Final layout of a chip.	42
27	Final layout of the wafer.	43
28	Photo of the cryogenic system. In the center : the Dewar with on top an RF cable exiting from the flange.	45
29	Photo of the final chip.	46
30	Schematic of the electronic setup.	46
31	Measured spectrum (DC voltage on detector) of the chip + electronic setup. Integration time of 100 ms with a source power of 20 dBm and step of 1 MHz.	47

List of Tables

1	Errors made on the characteristic impedance calculation due to approximations. . .	23
2	Errors made on the resonance frequency calculation due to approximations.	24
3	Table of the final layout chips theoretical properties.	44

Contents

Preface	2
1 Introduction	6
1.1 Introduction to cryogenics	6
1.2 State of the art in low temperature sensing	6
1.2.1 Thermistors and wired approaches	7
1.2.2 Wireless and minimal cabling approaches	7
1.3 Using MKIDs as temperature sensors	8
1.4 Research proposal	9
2 Derivation of an ideal design's specifications from a theoretical analysis	12
2.1 Optimizing the design with superconductivity theory	12
2.1.1 Introduction to superconductivity	12
2.1.2 Device noise analysis	14
2.1.3 Optimizing the superconductor cross-section	16
2.2 Exploring the superconductor possibilities	18
2.3 Exploring the dielectric substrate possibilities	19
2.4 Definition of waveguide specifications from microwave engineering	19
2.4.1 Derivation of the characteristic impedance	19
2.4.2 Matching the $50\ \Omega$ impedance with CPW theory	21
2.4.3 Tuning the resonance frequencies	23
2.5 Mitigating the loss mechanisms	25
2.5.1 Intrinsic losses	26
2.5.2 Coupling regimes	26
2.5.3 Radiation losses and parasitic modes	27
3 Development and characterization of fabrication processes	29
3.1 Resolution test structures used	29
3.2 Introduction to micro-fabrication processes	32
3.2.1 Photolithography	32
3.2.2 The film deposition by sputtering	32
3.2.3 Etching	33
3.2.4 Lift-off	33
3.3 Ion beam etching process	33
3.3.1 Superconductor deposition	33
3.3.2 Photolithography	34
3.3.3 Etching and resist stripping	34
3.3.4 Challenges encountered	34
3.4 Plasma etching process	35
3.4.1 Deposition	37
3.4.2 Photolithography	37
3.4.3 Etching and resist stripping	37
3.4.4 Challenges encountered	37
3.5 Lift-off process	38
3.5.1 Photolithography	38
3.5.2 Superconductor deposition	39
3.5.3 Lift off	39
3.5.4 Challenges encountered	39
3.6 Critical comparison of the processes	39
4 Realization of a multiple resonator network prototype	42
5 Cryogenic characterization of the devices	44
5.1 Measurement setup	44
5.1.1 Cryogenic system	44
5.1.2 Electronic instrumentation	44
5.2 Experimental data obtained	47
5.3 Discussion of the results	47

1 Introduction

1.1 Introduction to cryogenics

Since the first liquefaction of oxygen in 1877 by Cailletet and Pictet, the field of cryogenics has continuously aimed at reaching lower and lower temperatures. By using more sophisticated thermal machines, other gases were quickly liquefied, such as nitrogen and helium, enabling tremendous discoveries in low temperature physics. The latter has particularly enabled the discovery of superconductivity, a property of certain materials to drive DC electrical currents with zero resistance and expel the magnetic field from their bulk below a critical temperature.

Cryogenic technology has progressively found many industrial applications and with the more recent development of high temperature superconductors, has already or is set to revolutionize certain areas. We can quote for example the use of superconductors in electromagnets, which enable to drive very high currents and generate higher fields than permanent magnets. These have been used in particle accelerators such as CERN [5] or to confine plasma in fusion reactors such as ITER [6], and are more and more used in fMRI machines [7]. They also find applications as cables in electrical networks [8] as they allow low loss current transportation and a lower cable diameter. The same principle applies to power generators or converters [9] where smaller and lighter superconducting machines are critical for the aerospace industry or wind power generation. Lastly, the unlocking of sub-kelvin temperatures has enabled to cool systems in their quantum ground state, allowing many experiments in this regime and in particular the development of quantum computers [10].

All these technologies are enabled by placing the device inside a cryostat system cooled to the desired temperature and thermally insulated from the external world. This requires cautious thermodynamic engineering of the environment, whose basic principles are explained in [11] and will be quickly summarized here.

The main heat exchange mechanisms are radiation and thermal conduction through solid parts. Radiation heat exchange between two surfaces can be reduced by interposing a cooled third surface called a thermal shield, or by using a multilayer sandwich of reflective surfaces between insulators. The thermal conductivity of non metallic materials tends to decrease with the temperature as the average number of excited phonons tends to zero. On the contrary, this effect reduces the electronic scattering due to phonons, leading to an increase of electronic mobility in metals. Since heat conduction in metals is based on electronic heat conduction, their thermal conductivity is increased at low temperatures. Furthermore, the Kapitza thermal boundary resistance is especially critical since it can lead to temperature gradients at the interface between two materials.

These altered heat transfer mechanisms especially lead to problems because of the presence of numerous sensors inside the cryostat. These heat generating systems may have troubles evacuating their excess heat because of poor conductivity of their contact materials and create a local heat pocket. Also, due to incompatibility of control electronics with the cryo environment, the signals from these sensors have to be extracted out of the cryostat through metallic cables. These are packed in so called feedthroughs on the flanges of the cavity and constitute a privileged path for heat conduction inside the cryostat. Therefore, we can conclude that the temperature in such devices is far from being uniform.

Engineering constraints such as a maximum allowed temperature for proper device operation are essentially local. Indeed, in the case of superconductors driving high currents, it is absolutely critical that the superconducting phase be maintained everywhere. This problem is well known in the case of superconducting electromagnets as quenching [12]. A local transition to the normal phase with non zero resistance leads to quick heating of the material, thus propagating the quench by normalizing surrounding areas. If not quickly detected, it may be too late to apply countermeasures and the magnet will be damaged. Other local effects may include temperature gradients along long cryostats. This is because the coolant inlet is located on one side and due to finite heat capacity of the coolant, the cooled device may be hotter far from the inlet. This defines maximum acceptable temperature differences between different locations inside the cryostat [13]. This is especially critical in the case of superconducting cables that are by definition very elongated objects [14]. These issues emphasize the need for distributed cryogenic thermometry systems able to measure the temperature in different locations of the cryostat.

1.2 State of the art in low temperature sensing

Many different kind of cryothermometry systems have been proposed and commercialized, and will be reviewed here. But before going into a review of the state of the art, the sought after figures of

merit for such a device will be introduced. An interesting and detailed list can be found in [15] which will be summarized and completed here. The first item is resolution, i.e. the finest measurable step in temperature. This depends both on the responsivity of the device, i.e. the derivative of the measured quantity against temperature, and on the noise of the device. Finally, the measure needs not to be biased. That is, minimal self heating and low thermal mass to avoid self biasing, insensitivity to the external environment that can be quite extreme in cryogenic systems. For example, high magnetic fields near magnets, vibrations in mechanical systems or radiation in accelerators. Also, the system must have a stable calibration point that will not drift with time. This is especially the case when a device is cooled down and heated up to room temperature, as mismatch in thermal expansion coefficients between the sensor and its substrate will induce mechanical stress. Usually, sensors undergo a few full thermal cycles until they stabilize. We may also consider second order figures of merit such as ease of use and calibration, low cost, the operating temperature range, thermal contact with the sample, size/spatial resolution and the thermal response time. This last point can be particularly important for resolving fast events.

1.2.1 Thermistors and wired approaches

Historically, cryogenic sensors have been mainly leveraging the thermoresistive effect, that is, the change of resistivity of a conductor with temperature. Metallic thermistors show a positive temperature coefficient of resistance (TCR) as phonons will scatter more the electrons at higher temperatures, while semiconductor thermistors show a negative TCR due to the decreased conduction band population at low temperatures. Among the first sensors to be used industrially were the platinum sensors, with a coiled Pt wire encapsulated in ceramic [16]. However, their calibration below 70 K is more complex and their geometric design is not well suited to ensure a good thermal contact with the sample. Another popular resistor was the Allen Bradley carbon resistor [17], slightly less sensitive but allowing lower temperatures to be more easily probed, down to 2K. However, they were not very reproducible [16]. Research then moved towards thick or thin film thermistors, well suited for increasing the thermal contact with the sample. Also, smaller dimensions and film thickness allowed a lower thermal mass and therefore faster response times. ZrN films were reported in [18] with a similar sensitivity and temperature operating range as carbon resistors. Zirconium Oxy-nitride (commercially known as Cernox[®]) [19] sensors were an improvement with higher sensitivities, lower measurable temperatures (down to 0.3 K). However these sensors are more sensitive to magnetic fields below 1 K and RuO₂ sensors [20] are preferred, while allowing probing down to 50mK. While thermistor measurement is still one of the most used technique, it has the significant drawback of needing an amount of cables proportional to the number of sensors, as most of them require 4 point measurement of resistivity. As stated before, this represents parasitic heat conduction through the feedthroughs, signal deformation due to thermal noise along cables and increased wiring complexity and solder failure risk.

There has been some other kind of sensors that are more rarely implemented, such as thermocouples [16] but it requires a stable reference temperature point. Plate capacitor sensors have also been tried [16] by using the temperature dependence of the dielectric constant. They are not sensitive to magnetic fields but show a poor reproducibility. Diode sensors take advantage of the forward voltage temperature dependence [21], they are readily replaceable by other units in case of failure but cannot operate below 1.4 K due to important self heating. It should be noted that these solutions still have the problem of needing a number of cables that grows linearly with the number of required measurement points.

One immediate solution addressing the feedthrough problem is to incorporate some electronics inside the cryostat. A cryogenic analog to digital converter (ADC) has been shown to operate from room temperature down to 4.4 K [22]. It allows to branch all the sensor analog output to the ADC while needing only one serialized digital output. A similar approach is to use a capsule heated to 85 K containing a standard ADC [23]. This allows to benefit from low temperature electronic mobility enhancement while avoiding carrier freeze-out in semiconductors. However, this solution represents an additional heat source inside the cryostat. While both these solutions also improve the signal integrity through digitization, they still require about as much wiring.

1.2.2 Wireless and minimal cabling approaches

The alternative to avoid a cabling amount linear to the number of sensors is multiplexed thermometry. Solutions using optical fibers have been developed, with the advantage of being insensitive to magnetic fields. One of the first implementations has been to use Bragg gratings produced by UV interference patterns [24]. The temperature sensitivity comes from the thermal expansion of the

fiber, changing the Bragg grating period and therefore the filtered wavelength. Bonding to more temperature expanded materials like PMMA increased the sensitivity. This allows to multiplex different filtered frequencies along the fiber. However, the sensitivity decreases with lower temperatures as thermal expansion becomes less important, so the use below 100 K has not been reported. Another approach is based on Rayleigh backscattering of photons [25],[26]. After manufacturing, each fiber has a specific impurity and defect pattern that produces a unique backscattered spectrum for each strain / temperature configuration. Characterizing the fiber's pattern may be long, but allows precise measurements down to liquid helium temperatures. Compared to Bragg gratings, this allows a higher spatial resolution, but there is a trade-off with time resolution as intensive computational power is needed to resolve the temperature profile along the fiber (In [25], 200ms response time for 5mm segment resolution has been achieved). Also, this technique is sensitive to parasitic strain. A recent study [27] has tested several types of interferometric systems down to cryogenic temperatures but they suffer from the same kind of trade off.

Wireless sensing solutions have also been explored, solving all the problems related to cables. Quartz sensors have been proposed [28], [29]. They are made of an antenna receiving an RF signal that resonates with the crystal due to piezoelectric effect. However, this makes it sensitive to mechanical vibrations, so cannot be well in contact and thermally coupled to the sample and also showed spurious resonances if not properly treated. A ferrite yoke sensor has also been proposed [30], but with the drawback of being sensitive to magnetic fields and showing a very high sensitivity below 50K. This is a problem since each resonator therefore occupies a large frequency range, leading to a long spectral scanning process and reducing time resolution. More recently, an interesting approach based on nitrogen-vacancy (NV) centers in nanodiamonds has been proposed [31]. This all optical technique is based on photo-luminescence under a laser excitation and allows to integrate the diamonds directly on the sample with a very fine spatial resolution. However, this technique can be still considered under development as it has yet not been tried below 85K. Also, optical readout implies line of sight measurement of the sensors, which can be considered a drawback compared to RF probing in complex geometries.

It can be concluded from this review that there exist a large choice of systems when it comes to measuring cryogenic temperatures, allowing one to select the most suited to a particular environment. However, not all of them have been commercialized yet and the market still remains dominated by thermistors, with their known massive wiring problem. Among the two alternative solutions that are optical fibers and wireless sensors, only the former has shown satisfying results to the point of being applied in real systems, i.e. quench detection. Therefore, there is currently a lack of alternative solutions to this system in minimal cabling approaches. This defines the need of developing new ideas, that in order to be superior to these approaches, will require insensitivity to mechanical vibration/strain and magnetic fields, be of small size to enable fast thermal response time and spatial resolution and allow good thermal contact with the sample.

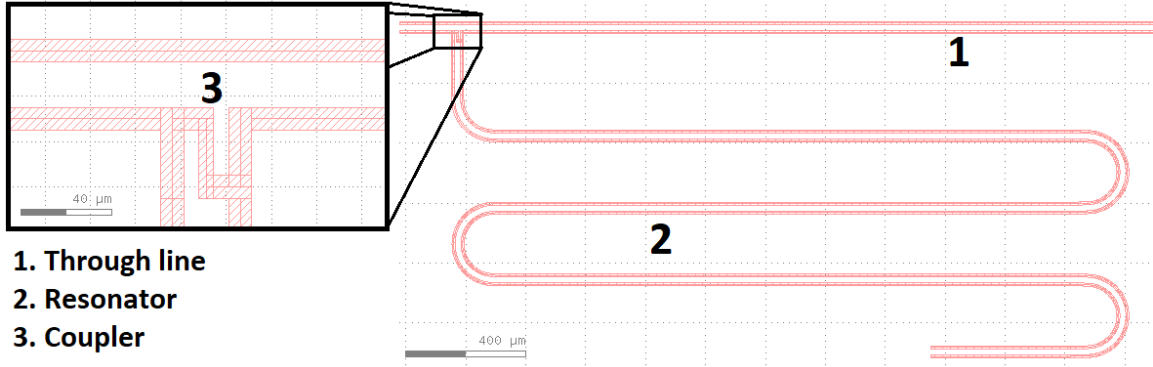
1.3 Using MKIDs as temperature sensors

In order to find a suitable new device for low temperature sensing with all the previously stated properties, it may be interesting to look at already existing concepts in other fields. A potentially interesting solution lies in the concept of superconducting Microwave Kinetic Inductance Detectors (MKID). This device has originally been proposed in [3] and [32] as a low temperature photon detector for low noise astronomic observation over a wide wavelength range. Their huge advantage compared to other superconducting photon detectors is that they are based on resonators, allowing to frequency-multiplex them into large addressable arrays with a single cryogenic HEMT preamplifier for the whole line. After nearly 20 years of continuous development, the device has demonstrated its suitability with the installation of a first MKID camera at the Subaru telescope [33].

A schematic of such a device can be found in fig. 2. The waveguide illustrated is a coplanar waveguide (CPW) with a central line separated by two gaps from the ground plane. The probing signal is carried by the through line and is capacitively coupled to each individual resonator. The resonators are $\frac{\lambda}{4}$ resonators shorted at their end. This provides a π phase shift by reflection at the shorted end, as well as by passing 2 times through the couplers and 2 times through the resonator length. Therefore, on resonance, the resonator creates a dip in the forward transmitted signal.

In the domain of photodetection, the working principle of MKIDs is explained in [3] and is illustrated in fig. 3. An incident photon with sufficient energy can break a Cooper pair from the superconductor and promote its electrons to the conduction band, they will be referred to

Figure 2: Sketch of a MKID layout (hashed red : substrate, white : superconductor). The signal is carried by the through-line and is coupled to resonators via the finger couplers.



as quasiparticles (panel A). The change in quasiparticle density changes the kinetic part of the resonator inductance, that is inductance linked to the momentum of Cooper pairs (panel B). This leads to a resonance frequency shift and a reduction of the dip amplitude due to losses attributed to quasiparticles flowing with a non zero resistance (figure C). Similarly, this leads to a phase shift on resonance frequency (panel D).

Summing up the detection scheme of MKIDs, it primarily detects a change in kinetic inductance due to a change in quasiparticle density from Cooper pair breaking. This breaking happened to be caused by absorbed photons in photodetection schemes. However, there are other means of breaking Cooper pairs, such as elevating temperature. Indeed, according to the Fermi Dirac statistic, the thermally excited quasiparticle density is a monotonically increasing function of temperature. A comparison of thermal and optical excitation has been carried out on a full Al MKID in [34], showing that for the same frequency shift, thermal excitations produced a slightly higher quality factor decrease. Also, it has been shown in [35] that the temperature dependence of the resonance frequency increases dramatically at temperatures closer to T_c . This proves that MKIDs could theoretically also be used as temperature sensors.

This would not be the first time that a temperature detector uses the kinetic inductance property of a superconductor. This concept has already been explored in [36] and [37] for the temperature sensing part of bolometers. The system is made of an inductive Wheatstone bridge running an audio frequency signal. One of the inductors is thermally connected to the photon absorber and another to a controlled heater, which enables differential temperature measurement.

Therefore, using MKIDs as an improved design would allow to probe large arrays corresponding to many different locations on the cryogenic sample with just two coaxial connections for signal input and output, similarly to optical fiber solutions. It should theoretically be less sensitive to mechanical strain, but its sensitivity to incoming radiation will have to be mitigated. Also, superconductors show a magnetic field dependence on their properties that will need to be investigated. Finally, CPW MKIDs can be patterned as thin films, enabling low thermal mass and good thermal contact with the sample, as well as a satisfying a good spatial resolution due to the device size. It shows promising perspectives for low temperature sensing.

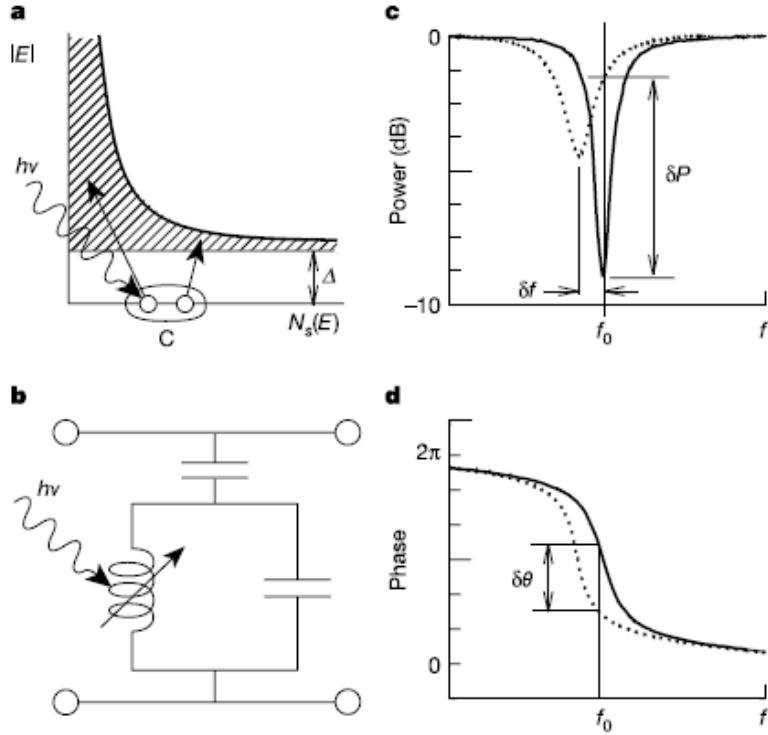
1.4 Research proposal

It has been demonstrated so far that for some cryogenic systems, a high spatial and time resolution distributed thermometry system was needed. Among all the cryogenic temperature sensors, only a few are able to realize such a system without needed extensive cable management. This defined the need for new minimal cabling approaches, and a theoretically possible candidate, the MKID, has been introduced.

To the best of our knowledge, even though the thermal response of MKIDs has already been studied in literature, there has never been an attempt to optimize its structure for temperature sensing. This defines the need to investigate further in this direction, in order to eventually commercialize functional sensors. This will require to explore possibilities with low temperature superconductors, high temperature superconductors, waveguide micro-structuring and other potential ideas to improve the device properties.

The work of this thesis takes place at the very beginning of this project. Therefore, we had to set realistic goals for the first milestone to be achieved. That is, choosing the design parameters

Figure 3: Illustration of the working principle of MKIDs, reproduced with permission from [3]. a. Electronic density of states of a superconductor against energy. Bottom conduction band energy is separated by Δ from the Cooper pair energy. b. Circuit equivalent representation of the resonator near its resonance frequency. The inductance varies with the density of excited quasiparticles. c. Frequency and amplitude shift of the resonance dip due to quasiparticle density increase. d. Frequency and phase shift of the resonance dip due to quasiparticle density increase.



(materials, dimensions), developing fabrication methods and placing a first low temperature superconductor device in the cryostat, running RF waves through it and study the transmission from the in-port to the out-port. This will allow to validate the layout design from a microwave engineering point of view, and have first pieces of data about the frequency temperature dependence.

This thesis is organized as has been the workflow of the project. The first part will provide an introduction to all the needed theoretical concepts to understand the theory behind MKIDs. A bibliographical work has been carried out to identify which materials would be best suited for our purposes and to set up guidelines to constrain the design parameter space. Then, fabrication techniques had to be investigated, in order to find the most suitable to match the design constraints. This is developed in the second part. The final part discusses the final layout that was adopted after the fabrication constraints have been taken into account, and how the chip is mounted with the cryogenic setup. Measurement data and their interpretation are provided as well.

2 Derivation of an ideal design's specifications from a theoretical analysis

In this section, we will proceed to a theoretical analysis of our device in order to specify guidelines for its design. We will first introduce the superconductivity theory and the sources of noise, to optimize the superconductor cross section. Then, we will discuss superconductor and dielectric material considerations. Microwave engineering constraints will follow to engineer the characteristic impedance and resonance frequencies. Finally, loss mechanisms and strategies for mitigation will be presented.

First of all, a few design choices needed to be made before digging deeper in the theory. It has been decided to use $50\ \Omega$ transmission lines as this is a standard for RF electronics compatibility with most commercial hardware. Also, among all the popular RF waveguide designs such as striplines, microstrips or single slotlines, the coplanar waveguide (CPW) design has been chosen. Its main advantages are ease of fabrication and extensive literature studying its properties for use in microwave technology.

2.1 Optimizing the design with superconductivity theory

This section will first present a brief introduction to the theory of superconductivity and the expected intrinsic sources of noise before applying some results to choose the best transmission line geometry.

2.1.1 Introduction to superconductivity

This section will first bring a brief overview of the superconductivity theory. Its mathematical developments are very complex and would require an entire book to be properly introduced, such as [38]. This is why this section will only state the main properties of superconductors in a simplistic fashion, while important analytical results for our engineering task will be reported more thoroughly. First, zero DC resistance will be understood as well as the superconductor band structure, then the Meissner effect will be explained, the two superconductor behavior under an applied field will be shown and finally the surface impedance will be introduced.

Zero DC resistance and band structure

The first striking property of superconductors is their ability to drive DC current with zero resistance below a critical temperature T_c , for which a phase transition takes place. According to the first principle superconducting theory by Bardeen, Cooper and Schrieffer (BCS theory) [39], electrons are coupled to the crystalline lattice. Therefore, they are able to exchange virtual phonons through lattice deformation, resulting in a positive attraction force between two electrons, as opposed to the exchange of virtual photons resulting in the repulsive Coulomb force. The resulting attraction force brings the electrons to condensate into the so called bosonic Cooper pairs. The effect of this pairing is that the normal density of states is suppressed in an energy gap Δ around the Cooper pair level. The size of the Cooper pair can be intuitively represented by a parameter called the superconductive coherence length ξ , that is given in the frame of the BCS theory to be

$$\xi_{BCS} = \frac{\hbar v_F}{\pi \Delta} \quad (1)$$

with v_F the Fermi velocity. The Cooper pair can be broken upon absorption of an energy greater than 2Δ (because it requires to promote 2 electrons to the conduction band). The resulting density of states can be recalled from fig. 3 (a). This puts the constraint that the signals driven in the superconductor have to satisfy $\hbar\omega < 2\Delta$ in order for it to be transmitted without being absorbed. Using a similar reasoning with the thermal energy $k_B T$, one understands that Cooper pairs are unperturbed by small enough thermal fluctuations. This leads to the relation between the critical temperature and the energy gap at $0K$: $\Delta(0) = 1.764 k_B T_c$. The energy gap is a function of temperature, and $\Delta(T) \approx \Delta(0)$ for $T \ll T_c$, then drops quickly to zero near T_c . It is therefore very important to always operate in frequency ranges that are not absorbed at the working temperature. Once the Cooper pair is broken, it releases two quasiparticles that are free normal state electrons. The quasiparticle density against temperature is given as [32]

$$n_{qp}(T) = 2N_0 \sqrt{2\pi k_B T \Delta(0)} e^{-\frac{\Delta(0)}{k_B T}} \quad (2)$$

with N_0 the single spin Fermi level electronic density of states. This expression is valid for $T \ll T_c$. A plot of $n_{qp}(T)$ is given in fig. 5 (panel a).

London equations

Another famous effect of superconductors is the Meissner effect, that is the expelling of the magnetic flux from the material bulk upon the superconductor phase transition. This effect is described by using the London equations [40]

$$\frac{\partial \vec{j}_s}{\partial t} = \frac{n_s e^2}{m} \vec{E} \quad (3)$$

$$\vec{\nabla} \times \vec{j}_s = -\frac{n_s e^2}{m} \vec{B} \quad (4)$$

with n_s the superconducting pair density, j_s the superconducting current and e the elementary electron charge. The first equation tells us that superconductive carriers can be accelerated by an electric field without dissipation, and the second equation that a static magnetic field will induce current loops. This effect is substantially different than the Faraday's law of induction which is dependent on the time derivative of \vec{B} . If one applies Ampere's law to the second equation, one gets

$$\nabla^2 \vec{B} = \frac{1}{\lambda_L^2} \vec{B} \quad (5)$$

with $\lambda_L = \sqrt{\frac{m}{\mu_0 n_s e^2}}$ the London penetration depth. It can be understood that the current loops shield the magnetic field inside the superconductor, leading to an exponential decrease of its amplitude from the surface to the bulk, as is represented in fig. 5 (panel B). A useful expression is that of the temperature dependent London penetration depth

$$\lambda(T) = \frac{\lambda(0)}{\sqrt{1 - (\frac{T}{T_c})^4}} \quad (6)$$

which will allow us to understand later the variation of the geometric inductance of the CPW. Indeed, the surface inductance of the superconductor comes as a perturbation of the total inductance value of the CPW, that relies mainly on this geometric inductance and can be made to be temperature sensitive. Finally, in thin film superconductors, typically when the thickness $t < 2\lambda_L$, the London depth parameter is replaced by the 2D screening length, or Pearl depth $\Lambda = \frac{2\lambda_L^2}{t}$ [41] in the decay equation of the field inside the superconductor. This result arises because when the film thickness is comparable to the London penetration depth, the current density inside the superconducting film can be assumed to be constant over its cross-section, whereas in a thick film, it is only localized on the surface. This length can be dramatically increased by making thin films, which will be useful later.

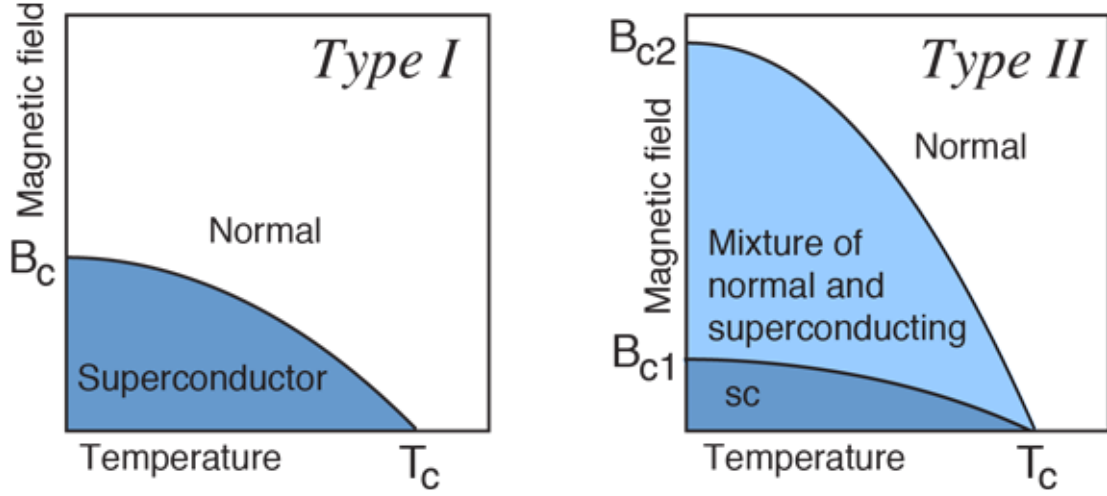
Superconductor types

Superconductors are split in two categories according to their magnetic behavior. Type I superconductors cease to be superconducting over a critical field H_c [42], while type II superconductors have two critical fields. Above the first one, magnetic flux will penetrate the bulk locally in the form of a normal phase vortex with a quantized flux. The second critical field has the same role as for type I. this behavior is represented in fig. 4. Usually, 0K critical field increases with an increased critical temperature. A direct consequence of the presence of the critical field is that carrying high currents through the superconductor generates a magnetic field which can exceed the critical field. Therefore, superconductors also have a critical current J_c associated, limiting the power that can be fed in the resonators.

Surface impedance

When driven with a high frequency signal, superconductors show a non zero surface impedance $Z_s = R_s + j\omega L_s$ [32]. R_s is the surface resistance due to the normal electron fraction, while $L_s = L_m + L_k$ is the surface inductance, with L_m the magnetic (or geometric) contribution found in non superconducting devices, and L_k the kinetic inductance. The magnetic field induced by the

Figure 4: Plot of the mean field type phase diagram for type I and type II superconductors. Reproduced from [4]



current and mechanical inertia of the Cooper pairs make up the surface inductance. The Drude model [43] for normal metals can describe kinetic inductance through the complex conductivity

$$\sigma = \frac{ne^2\tau}{m(1 + \omega^2\tau^2)} - j \frac{ne^2\omega\tau^2}{m(1 + \omega^2\tau^2)} \quad (7)$$

with τ the average collision time of electrons and n the carrier density. However, until terahertz frequencies, the imaginary part is negligible compared to the real part because of τ . In superconductors, as $\tau \rightarrow \infty$, kinetic inductance effects become observable. We can thus define a per length kinetic inductance by equating the kinetic energy to an inductive energy [44]

$$L_k = \frac{m}{2n_s^2} \frac{1}{A} \quad (8)$$

with A the cross sectional area of the superconducting film. The kinetic inductance fraction $\alpha = \frac{L_k}{L_m + L_k}$ is used to quantify the ratio of the varying part of the inductance to the usually bigger and constant magnetic inductance. Finally, in order to obtain the surface impedance, one needs first to compute the complex conductivity of the superconductor $\sigma = \sigma_1 + j\sigma_2$ [45]

$$\frac{\sigma_1(T)}{\sigma_n} = \frac{4\Delta_0}{\hbar\omega} e^{-\frac{\Delta_0}{k_B T}} \sinh(\eta) K_0(\eta) \quad (9)$$

$$\frac{\sigma_2(T)}{\sigma_n} = \frac{\pi\Delta_0}{\hbar\omega} \left(1 - \sqrt{\frac{2\pi k_B T}{\Delta_0}} e^{-\frac{\Delta_0}{k_B T}} - 2e^{-\frac{\Delta_0}{k_B T}} e^{-\eta} I_0(\eta) \right) \quad (10)$$

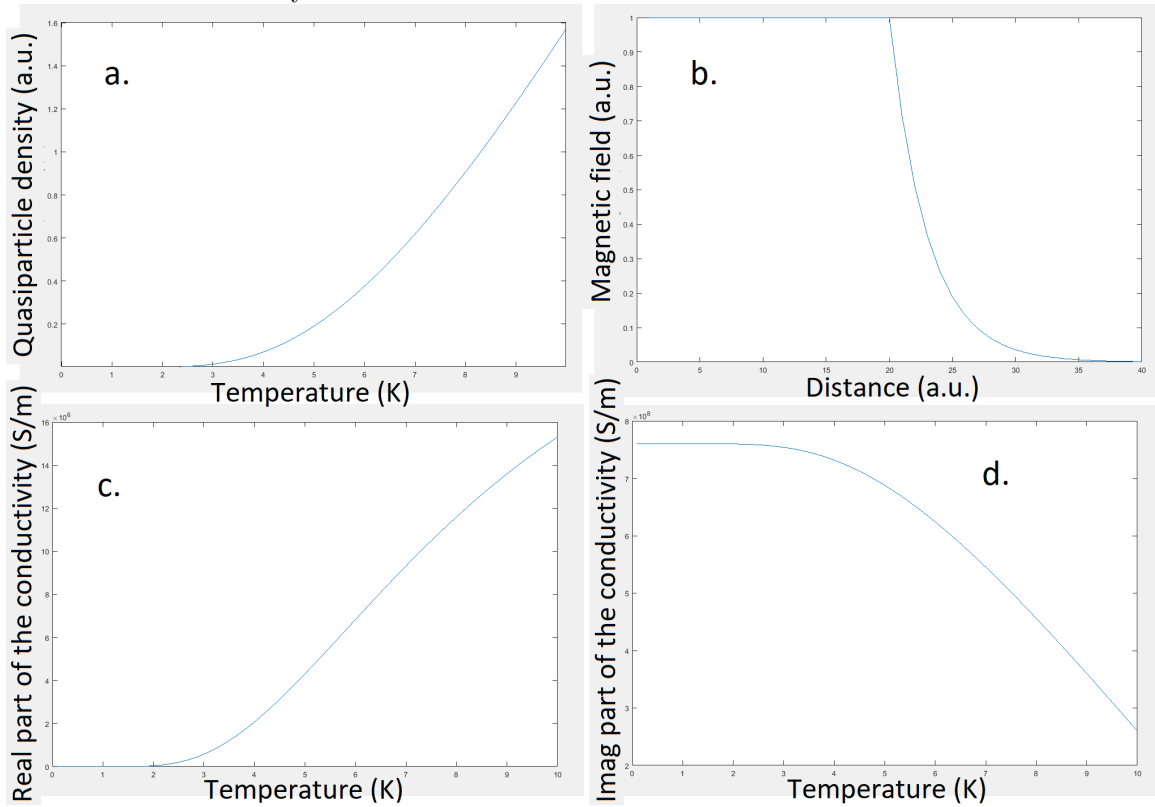
with $\sigma_n = \frac{ne^2\tau}{m}$ the normal metal Drude conductivity (in the low frequency limit), $\eta = \frac{\hbar\omega}{2k_B T}$ and I_n the n^{th} order modified Bessel function of the first kind, K_n the n^{th} order modified Bessel function of the second kind. These formulas are approximations for $\hbar\omega \ll \Delta$ and $k_B T \ll \Delta$, so the high temperature behavior may be inaccurate. Their plot against temperature are represented in fig. 5 (panel C and D). We will use later on these conductivities for computing the surface impedance Z_s .

This preliminary knowledge gives us clues as to how to optimize the sensitivity of the device. However, before trying to optimize it, we have to take into account the sources of intrinsic noise.

2.1.2 Device noise analysis

This section will introduce the expected sources of intrinsic noise, that is noise independent from the external electrical setup. Indeed, there will be supplementary noise sources linked to the input oscillator and electrical readout scheme, but this is out of the scope of this analysis. The noise can be divided in two components, that are the amplitude noise in the time domain and the phase (or frequency) noise in the frequency domain. Depending on the readout scheme, one or the other of these noises will be relevant. It should also be noted that noise is much less critical in temperature

Figure 5: Plots of equations of the superconductivity theory. a. Qualitative plot of the quasiparticle density against temperature. b. Qualitative plot of the magnetic field at the air-superconductor interface. Superconductor is after the abscissa 20 a.u., with a London penetration depth of 3 a.u. c. Real part of the conductivity, as given by eq. 9. d. Imaginary part of the conductivity. It was assumed that the material was being probed at 1 GHz, had a critical temperature of 10 K and the normal state conductivity of Nb at 10K.



sensing applications than in photon detection. Indeed, photon detectors are detecting transient events, so they are required to average out the noise on a time scale shorter than the quasiparticle lifetime, that can be as low as $1ns$ [46] up to the ms range [47]. On the contrary, state of the art temperature sensors like Rayleigh backscattering optical fibers [25] are resolving time scales of about $200 ms$, leaving much more time to take a measurement.

The lowest achievable noise is limited by the intrinsic generation and recombination noise. This is due to the fact that quasiparticles are randomly excited by thermal fluctuations or absorption of an incoming photon. At equilibrium, the recombination rate equals the generation rate, and the noise equivalent power (NEP) due to the generation-recombination has been derived in [32] as

$$NEP_{gr} = 2\Delta \sqrt{\frac{N_{eq}}{\tau_{qp}}} \quad (11)$$

with N_{eq} the equilibrium number of quasiparticles in the resonator, τ_{qp} the average quasiparticle lifetime and Δ the superconducting energy gap. The noise equivalent power is the power required to have a signal to noise ratio of 1 with half a second of signal integration time. We obviously expect the number of equilibrium quasiparticles to increase with temperature, as shown in eq. 2. This noise is expected to impact both the amplitude and frequency noise since both components of the surface impedance are functions of the number of quasiparticles.

An additional source of noise is found to be the coupler to the through line. Indeed, at such microscopic scales, the capacitance is expected to be quite low and therefore the Johnson thermal noise is enhanced. Indeed, as only a few electrons are hired for the charging of the capacitor, it becomes sensitive to thermal fluctuations, as given by the RMS noise voltage [48]

$$V_{RMS} = \sqrt{\frac{k_B T}{C_c}} \quad (12)$$

However, besides these fundamental noise sources, research in superconducting resonators has pointed out the presence of excess frequency noise one or two order of magnitude higher than the fundamental limit [45]. It turns out that the excess noise is due to two level systems (TLS), that are tunneling states in amorphous solids [49]. The amorphous state provides a wide range of available energies, thus parasiting in a wide range of frequencies. A historical review of experiments about TLS is proposed in [45], and we are going to condensate the main results.

The TLS have been found not to be related to bulk properties of the substrate or the superconductor, but are rather localized on interfaces. It is thought that they can form in native amorphous oxides at the surface of certain substrates or superconductors. They can also be related to amorphous process residues, especially after chemical etching processes. Power and temperature dependence of the TLS induced noise has been investigated in [45] and found to be for P the power $P^{-0.5}$ and T the temperature T^{-2} . These dependencies can be understood by the fact that these TLS come in limited numbers and therefore quickly saturate at higher powers or temperature. However, the use of too high powers is prohibited as non linearities will appear as the current is increased towards its superconductor critical value. Furthermore, it has been shown in the same study that the noise was following a $w^{-1.6}$ law, with w the width of the central line, for a constant characteristic impedance of the line. This translates in a proportionality with the gap width, and a smaller gap with the same power as a wider gap has a greater electric field, triggering TLS.

Now that the noise sources have been presented, it is possible to optimize the superconductor cross section to enhance sensitivity while mitigating noise.

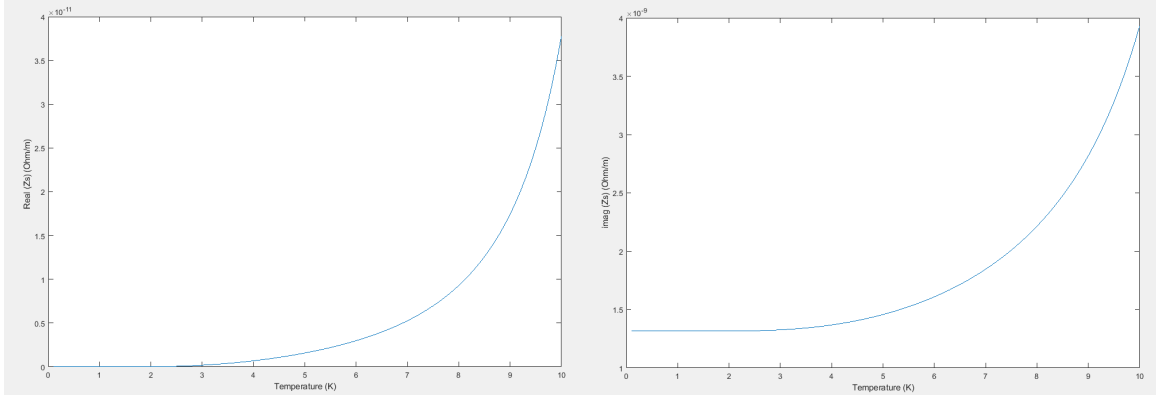
2.1.3 Optimizing the superconductor cross-section

After having explained the main results of the superconductivity theory and the noise sources, this section will provide arguments to allow us to choose the cross sectional dimensions of the waveguide. Indeed, it has been seen that some properties depend on the thickness of the film, while some others depend on the lateral width of the film.

First, we are going to discuss the pros and cons of reducing the film thickness. It has been derived in [45] that the per length impedance Z_s follows

$$Z_s = \frac{w}{(\sigma_1 - j\sigma_2)t} \quad (13)$$

Figure 6: Theoretical superconducting line impedance per unit of length. Left : real part, right : imaginary part. This was calculated using 9. A 1 μm line with 100 nm thickness and 50 Ω impedance was used. It was assumed that it was being probed at 1 GHz, had a critical temperature of 10 K and the normal state conductivity of Nb at 10K.



with σ the complex conductivity, t the film thickness and w the central line width. The theoretical real and imaginary parts of Z_s for a 50 Ω line of central width 1 μm and thickness 100 nm have been plotted in fig. 6.

It appears immediately that using thinner films enhances Z_s and therefore the kinetic inductance L_k . This can be understood using the results from the previous superconductivity theory chapter. Indeed, when going down below $t < 2\lambda_L$ the film is completely penetrated by the magnetic field and the London depth is replaced by the Pearl depth Λ . The latter being deeper than the former, it means according to the London equations that the superconducting carrier density is lower than in thicker films, resulting in a higher kinetic inductance. Using the ratio of the Pearl depth to the half central line width $R_\Lambda = \frac{\Lambda}{0.5w}$, it has been shown in [50] that the kinetic inductance is increasing faster than the geometric inductance with R_Λ , being equal for $R_\Lambda = 1$ in the case of infinitely narrow gaps. This indicates that the kinetic inductance fraction α increases with R_Λ . [32] has found that 40 nm MKIDs show about 100 times higher sensitivity than thick 320 nm ones.

However, there are a few drawbacks to thin films. First, the non-linearity threshold of the internal power of the resonators is decreased, leading to an increase in TLS relative impact and higher phase noise [32]. Also, in some superconductors, going too thin may induce unexpected changes in some parameters such as the critical temperature. Indeed, a different crystalline phase may be grown during deposition, and a potential native oxide in the order of a few becomes comparable with the superconducting film thickness, leading again in TLS impact. Finally, it is thought by the author that lower thicknesses lead to increased photosensitivity, which is not desirable for our application. Indeed, the radiation stopping power of a film is non-linear with its thickness since it decays as an exponential. Therefore, dividing by two the thickness of the film leads to less than a halving of the absorbed photons while dividing by more than two (if taking into account the non linear Pearl effect) the absolute number of superconducting carriers. As a result, the same photonic irradiation should break a higher relative amount of the Cooper pairs.

Then, the effect of a reduced central line width will be investigated. The drawback is that as stated previously, excess noise is enhanced when reducing the width. The advantage of using low dimensions is that R_Λ is increased, leading to an increase in the kinetic inductance fraction. This has been investigated in [46], building submicron resonator widths. They reported a mild improvement in sensitivity of NbTiN sensors because the responsivity was scaling faster than the noise power. Finally, it is explained in [32] that radiation losses are reduced with a larger width, as it follows a width w law w^{-2} . A good trade-off is to use a hybrid design with a large width near the resonator coupled end, where TLS effect is enhanced by the high electric field, and a narrower line at the other end where current and therefore sensitive inductive effects dominate [45].

Trying to reduce the width of the line leads to reducing the width of the gaps for maintaining the characteristic impedance. This can lead to a relative enhancement of the contribution of the magnetic penetration depth inside the superconductor relatively to the open area. Therefore, it gives a means of increasing the temperature sensitivity by using the magnetic inductance as well, but at the cost of potentially increasing the electric field between the line and the ground planes, enhancing the TLS activity.

As a conclusion, the design choice that will be made is a 150 nm film for a first design, not risking too high noise nor sensitivity. A future study of lower thickness resonators will be planned. We won't either try the hybrid design for the first run, but will aim at the lowest line width and gap width possible using optical lithography, to increase temperature responsivity. Now that the dimensions have guidelines, we still need to choose the materials that will be used before determining the final dimensions.

2.2 Exploring the superconductor possibilities

This section will deal with the parameters to consider when choosing a superconductor, and the possible choices. We first have to define what we are looking for to qualify a superconductor for our application and then we will review the most popular superconductors for MKID applications.

The first parameter to consider is the critical temperature of the superconductor. Indeed, a high critical temperature will allow a wider operating range for the thermometer. Also, as explained in the superconductivity theory part, a higher T_c is linked to a higher H_c , thus making our device more resilient in environments with a magnetic field and allows higher powers in the resonators before seeing magnetic non linearities, thus decreasing TLS impact by increasing the power. Finally, the author thinks that a higher critical temperature allows the device temperature to be more linked to the sample it is attached to than to the temperature of the remainder of the cryostat. Indeed, the device temperature is impacted by contact with the sample and absorption of black body radiations from other elements of the cryostat. Using Wien's displacement law, one finds that the black body emission peak energy is at $T \times 6,85.10^{-23}$ J, and equating it to the required energy to break a Cooper pair, one gets $T_{cutoff} = 0.71T_c$, with T_{cutoff} the temperature for which the maximum black body emission energy is below the superconducting gap. So, a higher T_c should decouple the device temperature from that of further parts of the cryostat and have a measurement more linked to the actual temperature of the contact sample.

The superconducting energy gap can also be used to build more sensitive MKIDs. Indeed, as reported in [45], one can build a two section resonator, with the inductance sensitive tip made of a superconductor with a lower energy gap than the superconductor used for the rest of the resonator. As an effect, quasiparticles diffusing in the tip will be trapped there, thus increasing the density of quasiparticles on the tip and increasing the sensitivity. However, depositing two superconductors makes the process more complex, and a first test device will not include such a structure.

Another important parameter for our application is the London penetration depth λ . Indeed, the higher it is, the higher the kinetic inductance fraction α will be, and therefore the more responsive the device will be. It also enhances the effective magnetic gap width as the magnetic field will be able to penetrate further in the superconducting edges, increasing the inductance of the transmission line.

The last parameter that will be considered is the quasiparticle lifetime τ_{qp} . Indeed, in photodetection schemes, one is looking for the longest τ_{qp} possible to be able to detect transient events in the excess quasiparticle density. This is not our case since we are interested in equilibrium quasiparticle density and therefore have interest in seeing the excess density from such transient events vanish as quickly as possible, to have the lowest impact possible on the averaged measure. Excess quasiparticles generated by high energy photons in radiative environments like particle accelerators will indeed be seen on the measurement as a false increase in the sample temperature. The downside is that a short τ_{qp} will increase the generation-recombination noise, but this is not a problem since it is expected to be anyway largely overshadowed by TLS or readout electronics noise.

A review of popular superconductors in the field of MKIDs can be found in [47]. Out of all the proposed superconductors, NbTiN is the one that corresponds the most to our criteria. Its critical temperature is of 15 K, much higher than most of the superconductors traditionally used. Even though its critical temperature is lower than for MgB₂ or YBCO, it has shown intrinsic quality factors 2 or 3 orders of magnitude higher than these materials. It also benefits from the shortest τ_{qp} of the list, in the order of 1ns [51]. NbTiN is usually used in photo-detector MKIDs as a material for the electric field dominated part of the resonator near the coupler for its low loss, another superconductor with longer quasiparticle lifetime being used for the inductance sensitive tip. We can exploit its properties for the whole resonator since we are not interested in the lifetime of the quasiparticles.

We can therefore say that NbTiN is the most suitable superconductor for our application, among the non exhaustive MKID candidate pool. However, for practical reasons, we will instead use NbTi for the first device. Indeed, the deposition of a film of NbTiN is a complex process and is outside the scope of this thesis. This superconductor has a critical temperature in the order of 9 K , allowing signals below 661 GHz at 0 K to be transmitted without absorption. The quasiparticle lifetime has not been reported in literature as this superconductor has never been tried for MKIDs. Also, the London penetration depth of bulk NbTi has been reported to be in the order of 150 nm to 200 nm below 6 K [52]. Now that the superconductor is chosen, we can choose a substrate material.

2.3 Exploring the dielectric substrate possibilities

This section will review the dielectric substrates that have been used in the literature to choose the most convenient one.

We only require that the dielectric constant be sufficiently large and not decreasing with temperature, and the dielectric losses small. The former is justified by the fact that, as will be seen in the next sections, the central line to gap width ratio to match the $50\ \Omega$ impedance depends on the dielectric constant of the substrate. If this one is too small, this leads to very large central lines and we may not benefit for the increased sensitivity of narrow lines. Also, as the inductance is expected to increase with temperature, having a dielectric whose dielectric constant decreases with temperature will counterbalance the inductance effect on the resonance frequency, while worsening the characteristic impedance shift. The latter requirement is essentially linked to the low TLS concentration of the substrate.

We will compare the two most popular substrate choices for MKIDs, and also the only ones we have available, that are Si and sapphire. In [53], sapphire and mono-crystal Si have been shown to have the lowest dielectric losses. In [54], sapphire was also reported to be the least lossy among materials (Si was not considered). [32] obtained higher quality factors with Si than sapphire, but the reverse happened in [35]. Si has a native amorphous oxide on its surface that is prone to host TLS, but sapphire is a crystalline oxide, so it should not be expected to host many TLS, leading to the hypothesis that higher losses reported in sapphire may be process dependent. So we can say that sapphire may have less losses if processed correctly. Furthermore, Si and sapphire wafers considered share a close dielectric constant, around 10, with sapphire being anisotropic (9.5 to 11.5 relative dielectric constant according to the crystallographic axis). It has been reported in [54] that sapphire has a monotonic positive dielectric constant temperature dependence. Intrinsic Si has been shown in [55] to have a negative temperature dependence, and boron doped Si showed a negative one at $T < 20\text{ K}$ with a very strong positive one between 20 and 30 K . Sapphire will therefore be preferred for processing related reasons, as well as for its dielectric constant temperature dependence. Indeed, it shows lower etch rates compared to Si in the process flows detailed in section 3, reducing the risk of over-etching the substrate and changing the impedance and resonance frequencies of the waveguide. Also, since we will consider several process flows, it will be possible to investigate fabrication related loss performance.

Now that both the superconductor and substrate have been chosen, it is possible to consider microwave engineering aspects to choose the last geometrical parameters, as will be done in the next section.

2.4 Definition of waveguide specifications from microwave engineering

After having fixed the materials that will be used and added a few constraints on the waveguide geometry, this section deals with the specification of the remainder of the geometric design space parameters. First, the notion of characteristic impedance will be derived and the study of the electromagnetic properties of CPWs will allow to choose dimensions matching a $50\ \Omega$ impedance. Then, the resonance frequencies will be derived in the case of a lossless transmission line. Finally, we will introduce the loss mechanisms and strategies to optimize the quality factor.

2.4.1 Derivation of the characteristic impedance

This first section will derive the characteristic impedance from transmission line theory. The basic results of transmission line theory can be found in any microwave engineering book, such as [56] or

Figure 7: Electrical model of a transmission line

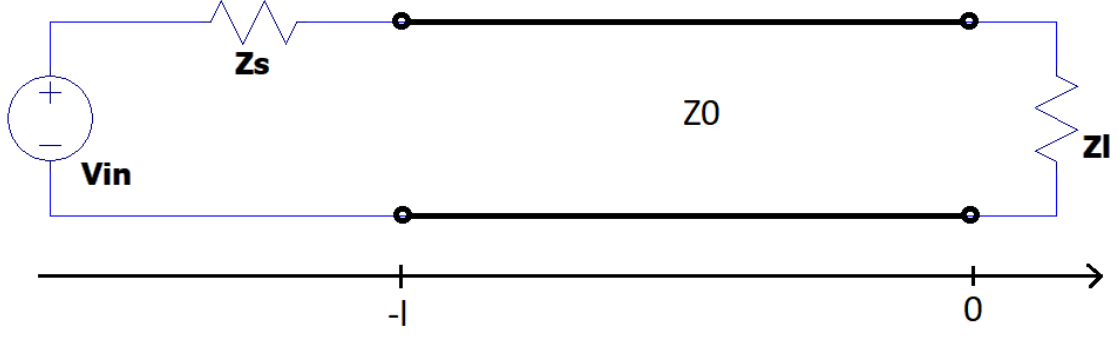
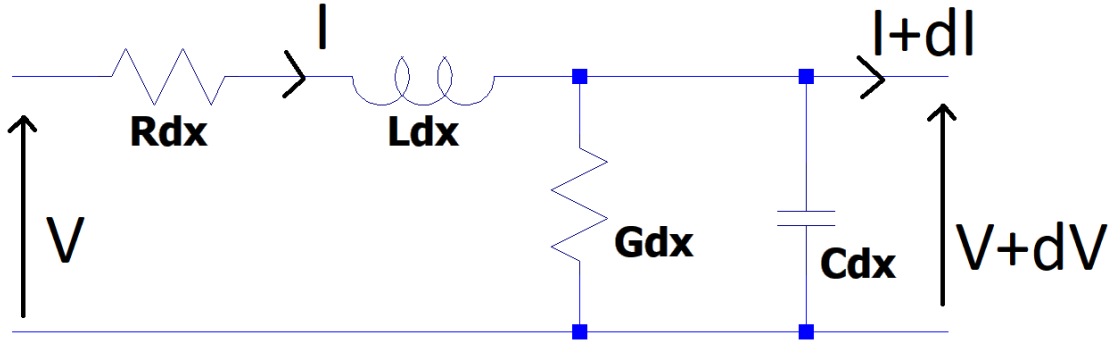


Figure 8: Differential section of a transmission line



[57] and will be summarized here.

The model of a transmission line can be found in fig. 7. We usually have a source impedance Z_s and a load impedance Z_l surrounding the transmission line with characteristic impedance Z_0 . Typically, for the through line of our device, the source and load impedances can be seen as the feedthrough coaxial cable impedances. Unmatched impedances will lead to voltage and current reflections, which needs to be avoided in the case of the through line, but will be needed later on for resonator lines.

We will assume that the voltage and current can be written as a Fourier series to solve each component independently.

We can model a transmission line from its infinitesimal segments, as shown in fig. 8 with lumped elements. The line section is made of a resistance Rdx and inductance Ldx in series, modelling the voltage drop through the section

$$dV = -(Rdx + j\omega Ldx)I \quad (14)$$

and a conductance Gdx in parallel to a capacitor Cdx shunted to the ground, modelling the current loss through the section

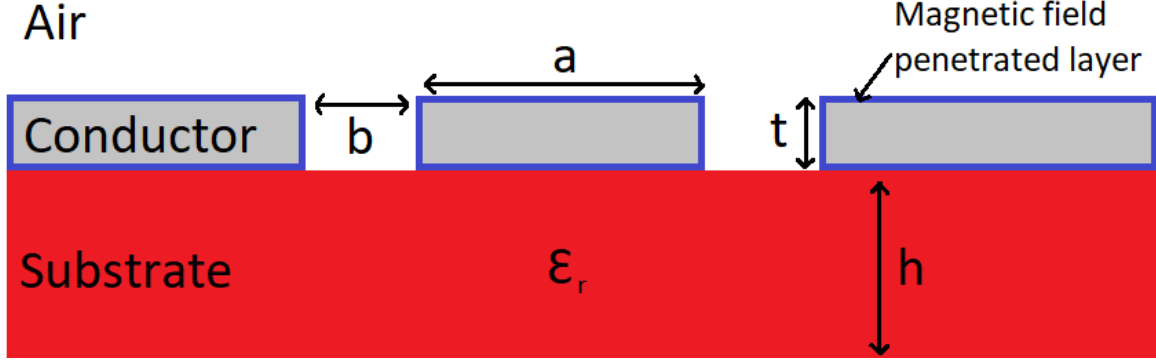
$$dI = -(Gdx + j\omega Cdx)V \quad (15)$$

These equations are known as the Telegrapher's equations. We can easily differentiate again eq.14 to inject eq.15 and obtain a wave equation

$$\frac{d^2V}{dx^2} = (R + j\omega L)(G + j\omega C)V = \gamma^2 V \quad (16)$$

A similar equation is obtained by doing so with the current equation, and the rest of the derivation is analogous and will only be carried for the voltage. The parameter $\gamma = \alpha + j\beta$ is the propagation constant with the real part being the attenuation constant and imaginary part the phase propagation

Figure 9: Cross sectional representation of a coplanar waveguide (without background ground plane). Dark blue represents the conductor surface region penetrated by the magnetic field (London depth).



constant. Assuming from now on that the transmission is lossless, since we will deal with losses in a future section, we can rewrite eq.16 as

$$\gamma \approx j\beta = j\omega\sqrt{LC} \quad (17)$$

Reminding that the voltage and current can be written in a Fourier series form, we can find for each pulsation a time-harmonic solution

$$V(x, t) = (v_+ e^{-\gamma x} + v_- e^{\gamma x}) e^{j\omega t} \quad (18)$$

$$I(x, t) = (i_+ e^{-\gamma x} + i_- e^{\gamma x}) e^{j\omega t} \quad (19)$$

Since these solutions still have to satisfy eq. 14, we can differentiate the voltage with respect to x and inject it with the equation of the current in eq. 14. Then, equating the constants of each matching exponential term leads to

$$j\beta v_+ = j\omega L i_+ \iff v_+ = \sqrt{\frac{L}{C}} i_+ = Z_0 i_+ \quad (20)$$

with Z_0 the characteristic impedance. A similar equation is obtained for the back-propagating terms. We now need to link the per length inductance and capacitance L and C to the CPW layout.

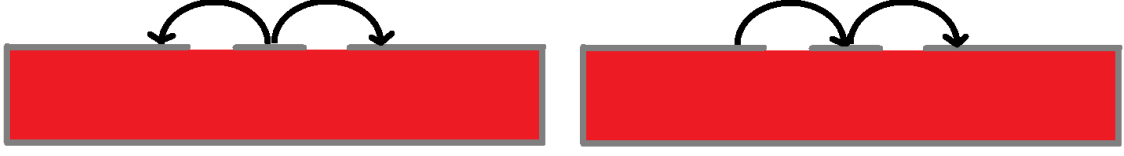
2.4.2 Matching the 50 Ω impedance with CPW theory

This section will briefly explain the mathematical methods employed to derive the per length inductance and capacitance of the CPW from its geometry. An interested reader can find a more in-depth and rigorous derivation in [58] or [45], while here focus will be given only to the main results. Then, the software tool used to design the CPW will be presented and results critically examined.

A cross-sectional view of the CPW geometry can be seen in fig. 9.

The following derivation is based on a few assumptions. First, the substrate is assumed to be isotropic. This is not the case of the chosen dielectric, sapphire. Then, the conductor is assumed to be lossless and the waveguide to carry a quasi-TEM mode. TEM modes are characterized by null longitudinal fields and null transverse currents. Since the dielectric has a different relative permittivity than air, the waveguide is vertically asymmetric. Furthermore, the surface impedance created by high frequency signals is not null. Both of these effects lead to non null longitudinal fields and transverse currents. But as shown in [45], these effects lead to very small components compared to the orthogonal components, thus the name quasi-TEM. Then, magnetic field penetration inside the superconductor is ignored. Finally, the superconductor thickness is assumed to be zero, which leads to simpler calculations and is justified by the fact that the superconductor thickness is about ten times smaller than the typical lateral dimension. Actually, it is still possible to make computations with a finite thickness as derived in [45] but the software tool used gives results independent of the film thickness. It should be noted that these results are only valid for the CPW mode. Indeed, as there are two gaps in this layout, the waveguide accepts two eigenmodes, i.e. the CPW mode with electric fields opposed in the two gaps, and the parasitic coupled slotline mode with electric fields

Figure 10: Illustration of the waveguide modes. The arrows represent the electric field. The substrate is in red and the metal in grey. Left : CPW mode. Right : coupled slotline mode.



in the same direction. The latter is excited when ground planes are not at the same potential. A schematic of these two modes can be found in fig. 10.

The electric field between the central line and the ground planes passes through the air half-plane and the substrate half-plane (for a null thickness), leading to

$$C_{tot} = C_{air} + C_{substrate} \quad (21)$$

One can see that calculating the capacitance between coplanar adjacent planes is non trivial. Therefore, in order to find an analytical solution, one has to use the technique of conformal mapping [59]. This technique based on complex analysis uses a function that takes a pair of coordinates in the geometrical space and remaps them to another pair of coordinates in a distorted space. There is an invariant property of the transformation that is the angles and shapes of infinitesimally small tiles. It is possible therefore to convert the coplanar geometry to a parallel plate geometry [45], which facilitates a lot the derivation of the capacitance. The width of the plates is found to be $K(k)$, with

$$k = \frac{a}{a + 2b} \quad (22)$$

and $K(f)$ the complete elliptical integral of the first kind

$$K(f) = \int_0^1 \frac{dx}{\sqrt{(1-x^2)(1-f^2x^2)}} \quad (23)$$

Similarly, the distance between the plates is found to be $K(k')$ with $k' = \sqrt{1-k^2}$. From here, we can easily derive the total capacitance of a parallel plate capacitor [45]

$$C_{tot} = \frac{1 + \epsilon_r}{2} \epsilon_0 \frac{4K(k)}{K(k')} \quad (24)$$

with ϵ_r the relative dielectric constant of the substrate. The total geometric inductance can be derived similarly, ignoring the contribution of kinetic inductance that is small enough not to perturb too much the value

$$L_{tot} = \mu_0 \frac{K(k')}{4K(k)} \quad (25)$$

Finally we can derive the characteristic impedance as

$$Z_0 = \frac{30\pi}{\sqrt{\frac{1+\epsilon_r}{2}}} \frac{K(k')}{K(k)} \quad (26)$$

In order to compute the characteristic impedance of the CPW, the online tool [60] has been used. It is based on the formulas and assumptions previously cited. The program has been fed with the substrate thickness (700 μm) and an effective relative permittivity for the sapphire taken at 10.5. It is found that using a ratio $a/b = 2$ approximately yields the desired 50 Ω impedance.

As previously explained, sapphire is anisotropic and the software requires an isotropic material. Computing the anisotropic behavior would require more complex calculations, for a marginal impact on the result. Indeed, using the same parameters that yield 50 Ω for $\epsilon_r = 10.5$, we obtain respectively 48 Ω and 52 Ω for $\epsilon_r = 11.5$ and $\epsilon_r = 9.5$, the two orthogonal values. Since the effective value lies between these two values, we can say that the middle point is a relevant approximation given the amplitude of the modification. Then, using a zero thickness approximation yields about 5% overestimation of the inductance and a 2% underestimation of the capacitance compared to numerical simulations according to [45] for a typical 3 μm central line CPW with film thickness 100 nm. This translates to a 3.5% overestimation of the impedance. Finally, by taking the case of a 2 μm central

line and a typical value for the London depth of 200 nm (It is reported in [52] that for bulk NbTi, λ_L is between 150nm and 200nm for a temperature below 6 K), we get according to the analytical formulas found in [50] an underestimation of 4% of the geometric inductance due to the ignored penetration of the magnetic field in the superconductor and an underestimation of 28% of the total inductance from not taking into account the kinetic inductance. These translate respectively to a 2% and 13% underestimation of the characteristic impedance. Overall, the zero kinetic inductance approximation seems to dominate. It should be added that deviations from the theoretical value will also be induced by the finite surface resistance due to high frequency signal and inevitable fabrication imperfections. All these results are summarized in table 1.

Approximation	L	C	Z_0	Comments
Substrate isotropy	0%	$\pm 4 \%$	$\pm 4 \%$	For ϵ_r as 11.5 and 9.5 instead of 10.5.
Zero thickness	+5%	-2%	+3.5%	Compared to numerical simulations.
Zero field penetration	-4%	0%	-2%	Using a 100nm λ_L .
Zero kinetic inductance	-27.5%	0%	-13%	Using a 100nm λ_L .
Total estimated error	-11.8%	-6% or +2%	-8.3% or -15.3%	Several values corresponding to the ϵ_r extreme cases

Table 1: Errors made on the characteristic impedance calculation due to approximations.

Now that the characteristic impedance has been evaluated, it has allowed to constrain the a/b ratio. This leaves us with the next geometrical parameter to define, that is the resonator length.

2.4.3 Tuning the resonance frequencies

In this section will be derived the resonance frequencies of lines of finite length l and connected to a load impedance Z_L at their end, Z_S at their source. Again, the interested reader can find supplementary information in [56] or [57].

By using the coordinates from fig. 7 and using $v = v_+ + v_-$, $i = i_+ - i_-$ we can write

$$Z_L = \frac{v(0)}{i(0)} = Z_0 \frac{v_+ + v_-}{v_+ - v_-} \quad (27)$$

It is now possible to derive a simple relation linking v_+ and v_- through a voltage reflection coefficient Γ

$$v_- = \Gamma v_+ = \frac{Z_L - Z_0}{Z_L + Z_0} v_+ \quad (28)$$

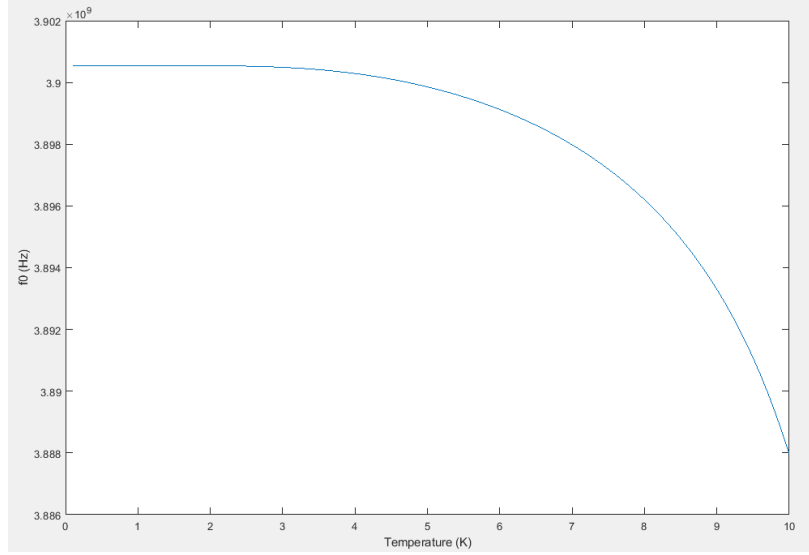
It should be noted that for a target characteristic impedance and load impedance of 50 Ω , a deviation of 1 Ω mismatch corresponds approximately to 1% of the voltage amplitude reflected. By using this reflection coefficient with the electrical length βl , we can define an input impedance Z_{in} seen from the input of the lossless line as if it was an equivalent load

$$Z_{in} = Z_0 \frac{e^{j\beta l} + \Gamma e^{-j\beta l}}{e^{j\beta l} - \Gamma e^{-j\beta l}} = Z_0 \frac{Z_L + jZ_0 \tan \beta l}{Z_0 + jZ_L \tan \beta l} \quad (29)$$

One can see from this equation that the reflection of the voltage at the end of the line modifies the perceived impedance by the maintaining of a standing wave inside the electromagnetic cavity.

For example, if we assume that we have a perfect reflection at the end of the transmission line (open-circuit or short-circuit), then $\Gamma = 1$ and $\Gamma = -1$, $Z_L = \infty$ and $Z_L = 0$ respectively. These two boundary conditions on the resonator induce or not a π phase shift on reflection, which defines the short ended resonator as a $\lambda/4$ resonator and the open ended resonator as a $\lambda/2$ resonator. We can see that for a shorted resonator, $Z_{in} = \infty$ on resonance and for this frequency the resonator is seen as an open end. For our design, the $\lambda/4$ resonator will be chosen since additional back and forth transmission through the coupling capacitors will add another π phase shift with respect to the through line signal to the signal leaking from the resonator to the through line, leading to a dip in transmission on resonance and an effective short circuit at the resonance frequency.

Figure 11: Theoretical variation of the resonance frequency with temperature. A 1 μm line with 100 nm thickness and 50 Ω impedance was used. The superconducting impedance used to compute the resonance frequency depends on the probing frequency, but is considered to be constant with small frequency variations. We have therefore used a probing frequency equal to the resonance frequency at 0 K (obtained after a few iterations). The superconductor was taken with a critical temperature of 10 K and the normal state conductivity of Nb at 10 K.



For a quarter wavelength shorted resonator, we impose $V(0) = 0$ and

$$\cos(\beta l) = 0 \iff \beta l = l\omega\sqrt{LC} = \frac{\pi}{2} + n\pi \iff f_0 = \frac{1}{2l\sqrt{LC}}\left(n + \frac{1}{2}\right) \quad (30)$$

One can observe several resonances being odd multiples of the fundamental frequency and therefore limiting the amount of available frequencies for other resonators in the array. There will however be a shift from the expected resonance frequency for the same reasons a shift from the expected characteristic impedance will be produced. Indeed, using a relative permittivity of 11.5 or 9.5 give respectively a 4% underestimation and overestimation of the resonance frequency compared to the case with $\epsilon_r = 10.5$. The zero thickness approximation yields a further 1.5% underestimation, and not including the London depth (typically 100 nm, but the exact value is not known) for the geometric inductance 2% overestimation. Lastly, not including the kinetic inductance yields a 7% overestimation. We therefore expect the actual resonance frequencies to be lower than the ones calculated. All these results are summarized in table 2. However, other effects linked to different waveguide modes in the waveguide turns may also contribute to increase the resonance frequency, thus counter acting the influence of the London penetration depth, as will be seen in the next section.

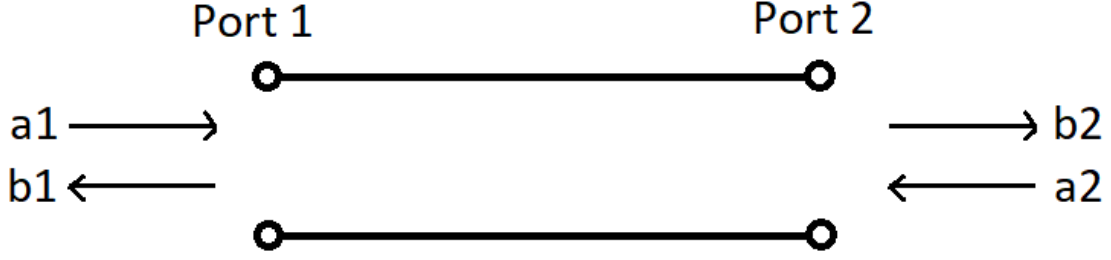
Knowing the equation of the resonance frequency allows us to add up the kinetic inductance and the geometric inductance (supposed to be constant, even though as a second order effect the effective gap width changes with the London depth). With the temperature varying total inductance, we are able to plot the variation of the theoretical resonance frequency against temperature curve in 11. The same dummy CPW as in the Z_s calculations was assumed, with a resonator length of 8mm.

Approximation	ω_0	Comments
Substrate isotropy	$\pm 4 \%$	For ϵ_r as 11.5 and 9.5 instead of 10.5.
Zero thickness	-1.5 %	Compared to numerical simulations.
Zero field penetration	+2 %	Using a 100nm λ_L .
Zero kinetic inductance	+11.7 %	Using a 100nm λ_L .
Total estimated error	+7.7% or +16.7%	Several values corresponding to the ϵ_r extreme cases.

Table 2: Errors made on the resonance frequency calculation due to approximations.

One should however take into account the effect of the coupling capacitor on the resonance frequency. Indeed, the whole device (coupler + resonator line) is seen from the through line (on the

Figure 12: Example of a two-port signal flow graph.



capacitor input) with an input impedance

$$Z_{resonator} = -\frac{j}{C_c\omega} + Z_{in} \quad (31)$$

with Z_{in} the input impedance of the line alone from eq. 29 and C_c the coupling capacitance. In order to find the resonance condition, we need to solve $Z_{resonator} = 0$. Due to the presence of the $\tan(A\omega)$ term, one needs to use a numerical approximation to find the solutions. We can intuitively retrieve for the perfect open $C_c = 0$ the same resonance condition as for the unloaded resonator, and for the connected line $C_c = \infty$, the direct short condition. By noting $\alpha = \frac{1}{C_c\omega_0}$, we can write with ω_0 the unloaded resonance pulsation and ω_r the loaded one

$$\omega_r = \omega_0 \frac{2}{\pi} \operatorname{atan}\left(\frac{\alpha}{Z_0}\right) \quad (32)$$

As an example, a line resonating at 1 GHz with a 1 pF capacitor leads to a reduction of the resonance pulsation of the ensemble of about 3%.

One can readily understand that in the quarter wave resonator the voltage is maximum at the coupled end and goes to zero on the ground plane end. The reverse is true for the current distribution. Since the main temperature dependent parameters are the inductances, we can see that the measured inductance shift will be mainly contributed by the region of the resonator near the shorted end. Therefore, even though resonator lines may be several millimeters long, the temperature sensitive part is essentially localized, allowing greater spatial resolution.

Since in our real device the resonator line is coupled to the through line with a capacitor, it does not necessarily have to be at 50 Ω . This can be used for example to enhance the amplitude of the voltage or the current and therefore enhance the impact of the related physical effects. One interesting move could be to enhance the current to have a detector more sensitive to the inductance, and less sensitive to the voltage excited dielectric impurities. But this would require using even narrower gaps, which is impossible when operating near the resolution limit of optical lithography, so this study is left for further developments.

These results were obtained in the case of a lossless resonator. Loss mechanisms will limit the sharpness of the resonance, as shall be seen in the next few sections.

2.5 Mitigating the loss mechanisms

After having treated the case of a lossless resonator, this section will introduce the loss mechanisms that are responsible for a non total suppression of the transmitted signal at the resonance frequency, and try to find solutions to optimize the losses.

We will first present an efficient way of representing RF networks with an arbitrary number of ports. These can be modelled through a signal flow graph, like in fig. 12.

The relation between the incoming waves \vec{a} and outgoing waves \vec{b} can be modelled through a so-called scattering matrix, or S-matrix, for which an example for the 2-port network is given :

$$\begin{pmatrix} b_1 \\ b_2 \end{pmatrix} = \begin{pmatrix} S_{11} & S_{12} \\ S_{21} & S_{22} \end{pmatrix} \begin{pmatrix} a_1 \\ a_2 \end{pmatrix} \quad (33)$$

Our system will therefore monitor the $S_{21}(\omega)$ parameter representing the transmission of the voltage amplitude from port 1 to port 2, and quality factors will be discussed for this signal.

A quality factor can be defined as the ratio of the energy stored in the resonator with the energy loss per cycle. It also represents the ratio between the resonance frequency and the resonance bandwidth, and a high quality factor is associated with a deeper dip at resonance. The total quality factor Q_{tot} can be defined as [32]

$$\frac{1}{Q_{tot}} = \frac{1}{Q_i} + \frac{1}{Q_r} + \frac{1}{Q_c} \quad (34)$$

with Q_i the intrinsic quality factor, Q_c the coupling quality factor and Q_r the radiation quality factor. The next sections will process these subfactors in that order.

2.5.1 Intrinsic losses

First, we will treat the case of the intrinsic losses of the resonator, that are the losses taking place inside the resonator, without accounting for radiative losses which will be treated later. We can define an unloaded quality factor $\frac{1}{Q_u} = \frac{1}{Q_i} + \frac{1}{Q_r}$ representing the losses ignoring the coupling.

In the previous section about lossless resonator lines, we have ignored the per length resistance R and leakage conductance G . We will still neglect G as we expect the superconductor to be completely etched from the gaps and the resistivity of sapphire is very high compared to the expected AC resistivity of the superconductor. Introducing R should slightly change the resonance frequency and the characteristic impedance, however since $R \ll \omega L$, we will neglect this effect.

Using eq. 29 and introducing the resistance, we can write an approximation of the input impedance near the resonance frequency as [32]

$$Z_{in} \approx \frac{4Z_0Q_i}{\pi(1 + 2jQ_i\frac{\Delta\omega}{\omega_0})} \quad (35)$$

with $\Delta\omega = \omega - \omega_0$. We can see that taking a very high quality factor leads to a very high input impedance on resonance, and a very small one even slightly off resonance, which is the expected behavior for the non coupled line. The intrinsic quality factor can be defined as the square of the ratio of the phase propagation constant to the attenuation constant [45]

$$Q_i = \frac{\beta^2}{2\alpha^2} = \frac{\omega L}{R} \quad (36)$$

The resistance R can be minimized by mitigating the dielectric losses as well as having a high quality superconductor that will not be lossy. However, intrinsic losses due to the superconductor are unavoidable as thermally excited quasiparticles induce losses. Now that the intrinsic quality factor has been introduced, we will define in the next section the coupling quality factor.

2.5.2 Coupling regimes

In this section will be discussed the coupling quality factor Q_c and its influence on the measured transmission on resonance. Indeed, the real device is the resonator line in series with the capacitor and we can therefore define a loaded quality factor equal to the total quality factor.

The coupling quality factor can be defined as the ratio between the energy stored in the resonator and the leakage through the capacitor per cycle [45]

$$Q_c = \frac{E_{stored}}{E_{leaking}} = \frac{\pi}{2\sqrt{Z_r Z_0} C_c \omega} \quad (37)$$

with Z_0 the through line impedance, Z_r the resonator impedance and C_c the coupling capacitance. The formula has been obtained by considering the tee-junction as a 3-port network in the limit of small coupling capacitances, i.e. $\omega C_c \sqrt{Z_r Z_0} \ll 1$. The coupling quality factor can be tuned by choosing properly the coupling capacitance C_c .

We can define another figure of merit for the resonator that is the insertion loss L_0 . Indeed, reciprocally to the energy loss of the resonator due to the coupler, not all the power impinging on the coupler from the through line is transmitted inside the resonator. L_0 is defined by the power loss between the through line power and that transmitted to the resonator. At equilibrium, the leakage power from the resonator is equal to the input power. This means that L_0 controls the relative amount of power that is transferred back in the through line with phase opposition, i.e. L_0 controls the depth of the resonance dip. L_0 can be calculated by [61]

$$L_0 = -20 \log\left(\frac{g}{g+1}\right) \text{dB} \quad (38)$$

with $g = \frac{Q_u}{Q_c}$.

According to the value of Q_c , we can distinguish two coupling regimes [61]. The first one, corresponding to a small capacitance is the undercoupled regime. It is characterized by a high coupling quality factor, therefore the total quality factor is approximately equal to its maximum limit, that is the uncoupled quality factor. However, the insertion loss is high and the depth of the resonance deep is shallow, which defines the need for a low noise amplifier on the electronic readout stage, such as a cryogenic HEMT [61]. The second regime is the overcoupled one, with a high capacitance leading to a low total quality factor defined mainly by Q_c . On the other hand, it has a low insertion loss and shows a deep resonance. When $Q_u = Q_c$, we are in the critical coupling regime, with a Q_{tot} half of its maximum value and an L_0 corresponding to half the power transmitted.

We have seen that the tuning of the coupling capacitance is an important step. We will aim for the critical coupling regime in our design since it shows the best trade off between quality factor and insertion loss. The next question to arise is how does the C_c value translate to a geometrical design. There are several possible designs with different impacts on the resonator properties. For example, [61] has found that in case one uses interdigitated fingers coupler, one has to take about 40% of the finger lengths to be added to the total resonator length to compute an accurate resonance frequency. Another important effect of the coupler is whether or not it creates a discontinuity in the ground plane by forming a tee junction.

2.5.3 Radiation losses and parasitic modes

This part will deal with the last loss mechanisms that are parasitic modes coupling. We will first quickly review the radiative losses due to coupling with free space, and then talk about the excitation of the coupled slotline mode.

Usually, radiation losses are small compared to dielectric losses in CPWs. However, for the sake of completeness, we provide here the formula for the radiation quality factor Q_r is [32]

$$Q_r = \frac{\pi(1+\epsilon)^2}{2\epsilon^{\frac{5}{2}}} \frac{Z_{void}}{Z_0} \frac{1}{I'(\epsilon, n)} \frac{1}{n-0.5} \left(\frac{L}{w}\right)^2 \quad (39)$$

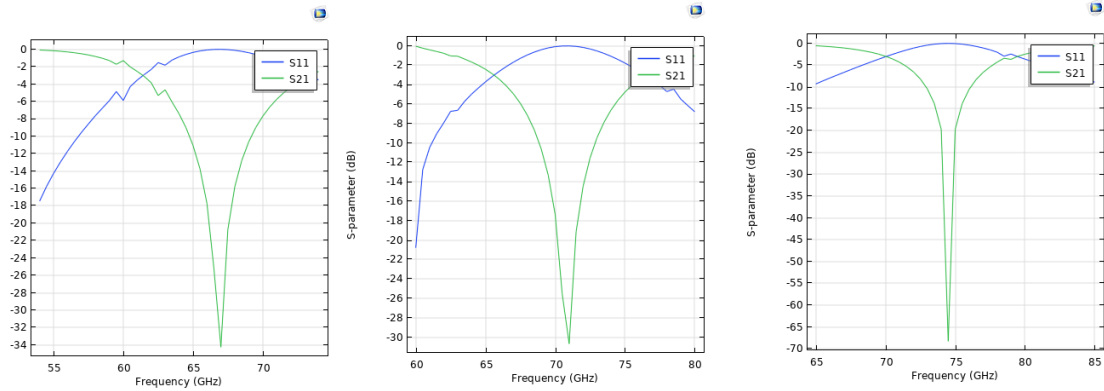
with ϵ the relative permittivity of the substrate, Z_{void} the impedance of free space (377 Ω), n the mode order, L the resonator length, w its width and $I'(\epsilon, n)$ a factor equal to 1.62 for the fundamental mode. As already stated before, a strategy to increase it is to decrease the central line width.

The second kind of parasitic mode is the coupled slotline mode. Indeed, as CPWs possess two symmetrical gaps, there exist two eigenmodes : the conventional CPW mode that shows symmetrical voltages and currents, and the coupled slotline mode with anti-symmetrical voltages and currents. It can be understood for the CPW mode that the ground planes are at the same potential while in the coupled slotline mode, they are at different potentials. Since the ground planes are connected at the input pads, only the CPW mode is excited. However, when comes a tee junction creating a discontinuity in the ground planes, for example with finger couplers, the coupled slotline mode is excited [62]. It can also be excited by asymmetric ground planes. RF engineers usually use air bridges by wire bonding to connect the two ground planes, but these wires behaves inductively or capacitively, changing in a hardly predictable way the behavior of the resonators [63].

The problem with this parasitic mode is that it does not share the same phase propagation constant as the CPW mode, resulting in spurious resonances visible on the transmission spectrum if strongly excited, and a shift in the CPW mode resonance frequency if partially excited along the resonator. Potential solutions include using an elbow coupler that does not break the ground plane [32] and using very wide ground planes to make a potential asymmetry less important [62]. This can be especially important between the resonator parallel meanders since the meander closer to the through line and to the end see asymmetrical ground planes.

Another way to excite the coupled slotline mode is to have a mode mismatch at the meander turns. Indeed, in [32], meandered resonators with small radius of curvature had a higher resonance frequency that that with bigger radius of curvatures and that without meanders. This means that somehow the meanders lower the phase propagation constant. We simulated on Comsol on CPWs with a central line of 4 μm and gaps of 2 μm . The total length of the resonators were always 500

Figure 13: COMSOL simulation of S parameters of CPW meandered resonators. Left : Straight resonator. Middle : resonator with one turn with a radius of 30 μm . Right : resonator with one turn with a radius of 15 μm



μm . The transmission parameters are plotted in fig. 13. It reproduces the increase in resonance frequency with the inverse of the radius.

One explanation to the shift in resonance frequency could be that a tight U-turn can no longer be seen as a CPW as its two gaps are asymmetric, leading to a quasi-even and a quasi-odd mode to which the CPW mode power will be split. These local modes have a different propagation constant than the CPW mode, leading to a shift in the resonance frequency. A possible solution is to use large turns and a spline coupling the straight lines to the curved sections to facilitate mode matching.

We have seen that some elements of the geometry are important to consider to avoid unwanted coupling to other modes. In case of a backside metallization of the substrate (which will be our case), another parasitic parallel plate mode can appear.

This preliminary theoretical analysis has already allowed us to define the ideal parameters for the resonators. However, there exist real life practical limitations imposed by the fabrication methods. This will be further developed in the next section.

3 Development and characterization of fabrication processes

Ideal design specifications have been established in the previous section. However, there exist practical limitations imposed by the tools used for fabrication. The aim of this section is to present the test structures used, the different fabrication methods that have been considered and their results, before going into a critical comparison.

First, although the superconductor material discussion concluded that NbTiN would be a good candidate material, it should be noted that the deposition process is quite complex compared to NbTi. Indeed, variations of the nitrogen partial pressure during the sputter deposition step lead to variations of the superconducting properties of the film [64]. Learning how to optimize the parameters of the sputtering machine as a non standard process to produce films with the desired properties is outside the scope of this master thesis, so the first device that will be fabricated will use stoichiometric NbTi.

Then, in order to qualify a process flow, a few figures of merit will be considered. First is the waveguide profile obtained, that is, in order to match as much as possible with the theory and avoid unexpected effects, how close the central line cross section is to a rectangle. Then, design faithfulness is to be considered, i.e. the minimum width achievable for which the ratio of superconducting line width to gap width is faithful to the design, in order to keep the $50\ \Omega$ impedance. Lastly, the cost of the process and chemical contamination are important. Indeed, chemical processes may alter the chemical composition of the surfaces, which can have consequences in terms of losses.

Among all the available processes, we can already disqualify some. Deep UV lithography in CMi requires the use of stepper masks, which is not compatible with first designs development, prone to frequent changes. Electron beam lithography also allows a great resolution but is a slow and costly process when applied to a whole wafer with different chips and is rather used for small samples with extreme resolution, so it is not really practical for our early designs. For the etching process, wet etching suffers from isotropic behavior, which is not compatible with the need to match fine lateral dimensions. This leaves us with 3 potential candidates, that will be reported in the next sections : lift-off, ion beam etching and chemical plasma etching. A schematic of the respective process flows can be found in fig. 14.

3.1 Resolution test structures used

This first section will introduce the resolution test structures that have been used to qualify the fabrication methods. Many different test structures have been patterned on the test samples, however we will only discuss the ones that were truly useful for our characterization.





The first test structure is the isolated line structure (fig. 15, panel a). The second one is the duty cycle dense lines (panel b). This one is intended to study if the lithographic process can pattern different line to width ratios. The third test structure is the finger coupler (panel c). Since the finger coupler is the critical dimension structure of the design, this test is especially useful. The last test structure is the L structure (panel d). It is intended to check the minimum gap dimension, in perpendicular directions. This is needed because the photolithography exposure tool scans in one direction, so we can expect some anisotropy close to the resolution limit.

Other test structures not related to resolution tests have been introduced. The first one is the 3-pad test structure (fig. 16, a.). It is made of a wide direct metal line between two ports, and the third middle port is separated from the metal line by a gap corresponding to the critical dimension of the design. In that way, assuming that the resistivity of a thin NbTi film is about the same as that from the bulk, we can compare the resistance from port 1 (left) to the other two ports and deduce the remaining non etched film thickness from geometric arguments. The second structure is a 4 pad one designed to make 4-wire resistivity measurements (fig. 16, b.). The last one is the end-point detection structure. It aims at detecting when the thin film to be etched has been completely removed. It has been observed that wide open areas have a higher etch rate than narrow gaps such as those in our design. So, an array of densely packed lines of the same dimensions as the critical dimension of the design has been put, as is depicted in fig. 16, panel c.

Now that the benchmark test structures have been introduced, the fabrication methods will be presented in the next sections.

Figure 14: Process flows (Lift-off and etching) for the fabrication of CPW

Lift-off process

Process description	Cross-section after process
<i>Lift-off PR coating</i>	
<i>Photolithography exposition & development + Descuming</i>	
<i>Metal DC Sputtering</i>	
<i>Lift-off PR stripping</i>	

Etching process






Process description	Cross-section after process
Metal DC Sputtering	
<i>Photolithography PR coating</i>	
<i>Photolithography exposition & development</i>	
<i>Metal Dry etching (Ion Beam Etcher / Specific chemistry)</i>	
<i>PR stripping</i>	

Figure 15: Schematics of the resolution test structures used. White : superconductor, red : substrate. a. Isolated line. b. Lines and gaps with different duty cycles. c. coupler. d. L structure.

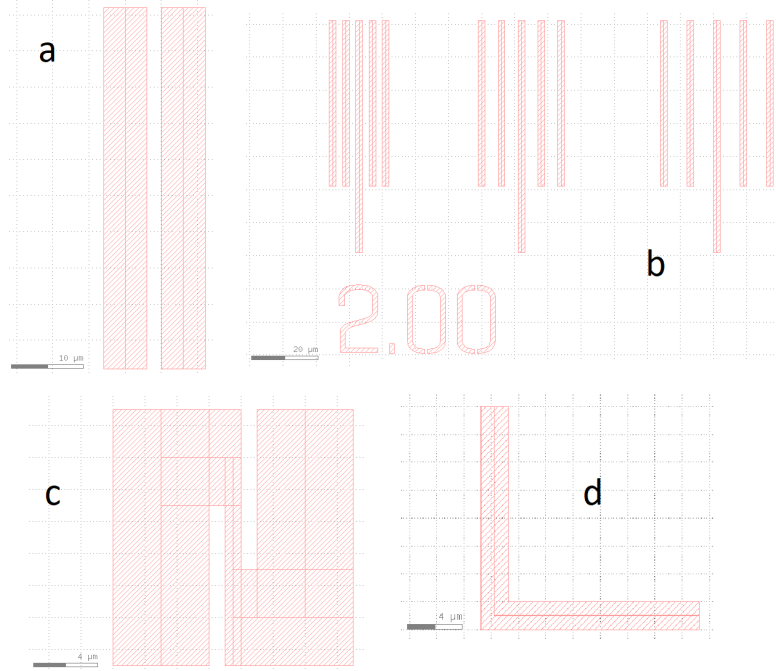
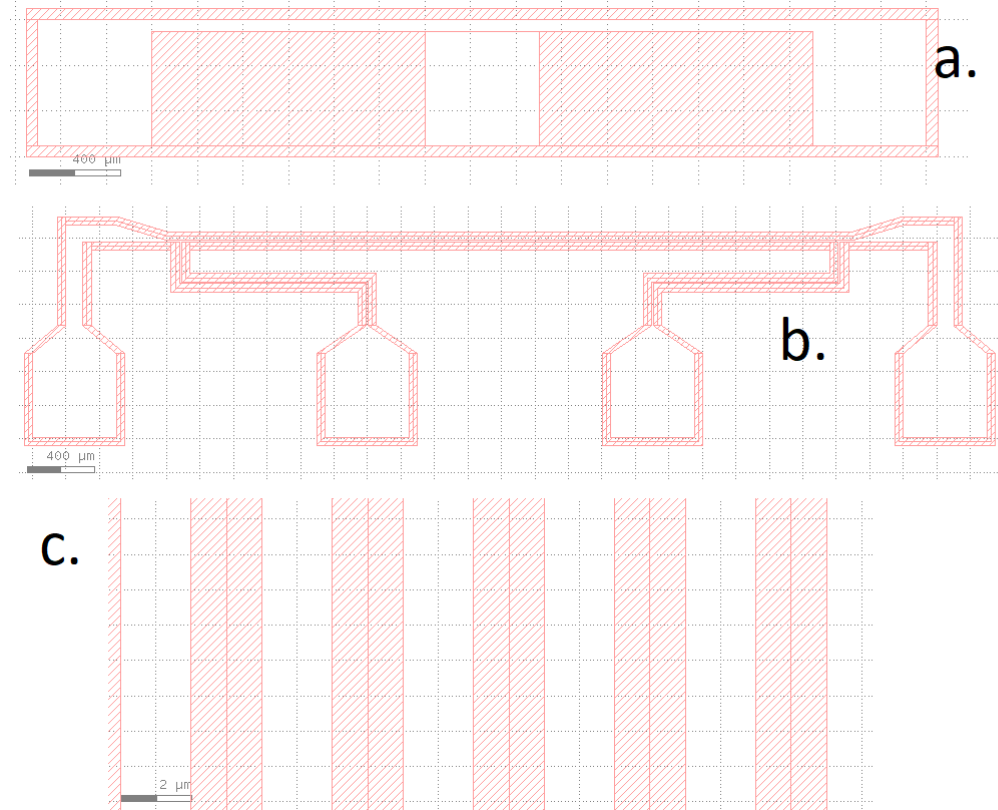


Figure 16: Schematic of the pad test structures. White : superconductor, red : substrate. a. 3-pad full etching detector. b. 4-wire resistivity measurement structure. c. Dense line endpoint detection structure.



3.2 Introduction to micro-fabrication processes

This section aims to provide a general overview of the methods used to fabricate micro-devices. The details of the parameters used for our specific process flows are given in the next sections. We will first introduce the method of photolithography, before explaining the two principal methods to transfer the photo-lithographic pattern on a film of another material. These methods are etching and lift-off.

3.2.1 Photolithography

Photolithography is a method used to pattern a layout on a layer of a material called photoresist. We will only use direct writing optical lithography in our processes, which excludes electron beam lithography and stepper optical lithography. The process is based on the optical exposure of a photosensitive layer called photoresist, which alters its properties. The resist is said to be positive-tone when its molecular bonds are weakened upon light exposure, and negative-tone when they are strengthened. The photoresist is a chemical mixture containing a photosensitive compound, a solvent controlling its viscosity and other compounds such as optical dyes.

The photo-lithographic process starts by a preliminary photoresist adhesion enhancement step, which can be a thermal dehydration or the coating of a layer of the adhesion enhancer HMDS. Then, the photoresist is coated, usually with a process called spin-coating. The photoresist is dispensed on the wafer that is rotating at a given speed. This rotation speed defines the thickness of the photoresist because the centrifugal force is competing against internal friction forces due to the resist viscosity. This step is followed by a soft bake, that is mainly aiming to evaporate the solvent from the resist [65]. This is important to improve the resist adhesion to the substrate and avoid the phenomenon of dark erosion during development. This is the process through which unexposed resist is still developed away by the developer, worsening the lateral dimensions fidelity.

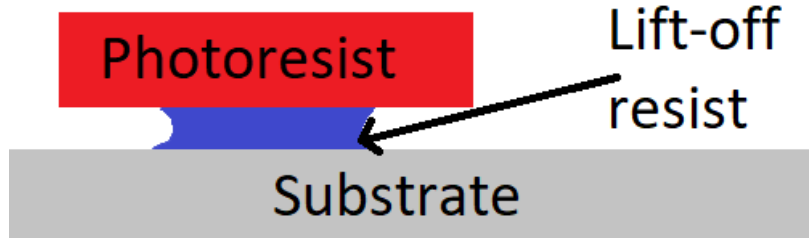
The next step is the optical exposure. It requires an exposure tool, in our case a direct writing one. The tool is a stage made first from a laser whose wavelength has to be chosen in the photosensitive range of the resist. Also, the dose has to be specified, that is the photonic energy per surface unit. If the dose is too low, the resist will not be developed after. If the dose is too high, theoretically unexposed regions near the exposed ones will start to be developed. The wafer moves under the beam, so the design is cut in stripes, typically with a field size 200 μm wide for the highest resolution in CMi. Each field contains a certain amount of pixels. On the exposure focal plane, the pattern that is projected is modulated from the raw beam by the pixel array. Then, a final lens focuses the beam on the substrate. The defocus parameter of the exposure tool specifies where the focal plane should be located, i.e. on the resist surface or inside its bulk. The final resolution achievable depends on the photoresist and the optics of the exposure tool, i.e. its depth of focus and numerical aperture. If the photoresist used is a chemically amplified one, it requires an additional post exposure bake [66]. This is because in this kind of resist, the photo-reaction needs heating to be completed.

The last step of the photolithography is the resist development, i.e. the removal of the exposed (or unexposed for negative resist polarity) resist. This is done using a specific chemical called the developer that has to avoid as much as possible dark erosion. This step can be followed by a hard bake. This step improves the thermal, mechanical and chemical stability of the resist for subsequent steps [67]. This is useful for example to protect the resist in aggressive physical sputtering processes such as ion beam etching. This can also be used to reflow the resist, i.e. soften the edges and make the resist walls inclined.

3.2.2 The film deposition by sputtering

Transferring the resist pattern on a layer requires the deposition of the layer to be patterned. The deposition of the film can be done using two wide families of processes named chemical vapor deposition and physical vapor deposition. In our case, we use only physical vapor deposition as NbTi deposition is only available for this process in CMi. The specific method used is called DC sputtering. The idea is that a NbTi target is placed on the cathode and the wafer to be coated on the anode. Application of a DC bias will then accelerate free electrons that will ionize an interstitial gas into a plasma state. The ions will be accelerated on the NbTi target that will sputter NbTi atoms in the cavity. These atoms will eventually deposit on the wafer with a good uniformity if the wafer is placed sufficiently far from the NbTi target.

Figure 17: Representation of the lift-off bi-layer resist structure after development.



3.2.3 Etching

In order to transfer the pattern obtained on the photoresist on an underlying film, one will use the etching method. Its complete process flow is depicted in fig. 14. After the initial deposition, the photo-lithographic process is carried out. Its dose and defocus have to be tuned in order to find the best parameters for the reflectivity of the underlying deposited layer. The etching process starts here. The goal is to etch the underlying film in the areas where the photoresist has been developed away. Two big families of process for etching exist : the wet etching and the dry etching. Wet etching is a chemical etching using a liquid and is often isotropic, therefore enlarging the patterned gaps, which does not fit our goal to have small lateral dimensions. The other family is dry etching processes that can have a chemical etching component and/or a physical sputtering component. They are usually more directional. The two etching methods we will use for our processes are the ion beam etching, a purely physical sputtering and the dry plasma etching, using a plasma that will chemically react with the underlying film.

The last step is to strip-off the photoresist in order to reveal the underlying pattern. This is usually done by a first oxygen plasma etching to remove the first nm of the resist that have been modified by the etching process and then use a chemical called remover that will strip the resist.

3.2.4 Lift-off

The lift-off process aims to transfer the photoresist pattern on a film that is deposited after the photolithography. This is shown in fig. 14. This requires to adapt the layout that will be patterned. Indeed, in order to pattern the same layout as for the etching process, one has to invert his design. A descumming step is carried out right after the photoresist development in order to ensure that the developed regions are resist-free. Indeed, as the next step is the deposition of the film, it is necessary to ensure that there will be no photoresist trapped below the film, to promote its adhesion and avoid surface topography.

After the film deposition, the proper lift-off step can be done. The idea is that the resist will be stripped off using the remover with the metal deposited on top, leaving an area blank of the deposited film. In order to do so, the lift-off resist used is a bi-layer stack, as depicted in fig. 17. The top layer is the photosensitive one, and the bottom layer is a sacrificial layer that will be under-etched during the development. This is to avoid that the film deposited on the resist vertical wall makes a bridge with the horizontal film. Sometimes sonication (ultrasonic agitation) is used to hinder resist adhesion to the substrate.

This closes this general overview of the fabrication processes. The next sections will introduce the specific machines and parameters used for each processes, as well as the challenges that had to be overcome.

3.3 Ion beam etching process

This section will present the workflow of the ion beam etching process (IBE).

3.3.1 Superconductor deposition

As a first step, the sapphire wafer has undergone a 10 minute Piranha cleaning to remove any organic contamination before the deposition.

Then, 150 nm of stoichiometric NbTi has been sputter deposited on the bare sapphire wafer using a DP650 machine [68]. The deposition took place at room temperature (20°C) under a pressure of

5 μ bar and an Ar flow of 30 sccm. DC electrode was used with 250 W power on a 100 mm target, with an average deposition rate of 0.3 nm/s. The NbTi layer showed good adhesion to the sapphire substrate after a Kapton tape stripping test.

3.3.2 Photolithography

The wafer was then thermally dehydrated as part of the photoresist coating process on the ACS200 coating machine [69]. A 0.7 μ m layer of the positive tone reflow optimized resist AZ 10XT-07 has been spin-coated (rotation speed of 5650 RPM). This resist was chosen because it is possible to reflow it and create inclined photoresist walls to avoid re-deposition during the ion beam sputtering process. The resist has then undergone a soft-bake at 120°C for 1'30.

Exposure was done with a 405 nm wavelength laser on an MLA150 direct writing photolithography machine [70]. This exposure tool is not the direct writer showing the best resolution, but this resist is only allowed on this exposure tool at the CMi. Exposure in another direct writing tool at the CMi is not recommended due to possible contamination of lenses. A dose of 145 mJ/cm² was used and a defocus of -2%. The defocus and laser wavelength were the ones recommended for this resist thickness. An optimal dose has been obtained by using a series exposure with different doses for a test Si substrate. However, no ideal dose is to be found for sapphire wafers as a field stitching problem on the exposure machine led to periodic underdevelopment patterns independent of the dose used. An image and height map of the pattern can be found in fig. 20. This is likely linked to a baking issue that is sensitive to the substrate material thermal and infrared properties.

Development was done with the same machine as for the coating, i.e. ACS200 with a 1:3.5 dilution of the developer AZ 400K in water. This developer is an organic solution based on KOH and allows a sharper edge profile. The resist was then reflowed by putting the wafer 2 minutes on a 125°C hotplate, before going for 16h in an 85°C oven for the hard bake. The reflow is an important step as ion beam etching sputters the wafer materials and can redeposit on sidewalls. Reflowing the resist then allows to make the sidewalls inclined, which are less likely to trap the sputtered materials, thus minimizing the so-called “fencing” effect. However, this imposes that the lateral geometry be at least three times larger than the resist thickness, i.e. at least 2 μ m and so puts a constraint on the minimum achievable lateral dimensions with no deformation.

3.3.3 Etching and resist stripping

The etching was done using the Veeco Nexus IBE350 Ar ion beam etcher [71]. The substrate fixture is kept at temperatures below 90°C and is rotating with a beam incident at 10° of the surface normal. The process consisted of exposing the wafer in these conditions for 10 minutes in the low power regime (300 V beam voltage, 500 mA beam current and an incident RF power of 500 W). The 10 minutes of total etching time were split in blocks of 30 s, separated by 10 s of cooling down. This is done to prevent resist overheating. The machine allows secondary ion mass spectroscopy endpoint detection, but the exposed surface was too low to detect any change in the ion concentrations with our trenches end point detector structures. Hopefully the etch rate of NbTi had previously been found to be 25 nm/min due to end point detection with large open areas on a dummy wafer with our etching configuration.

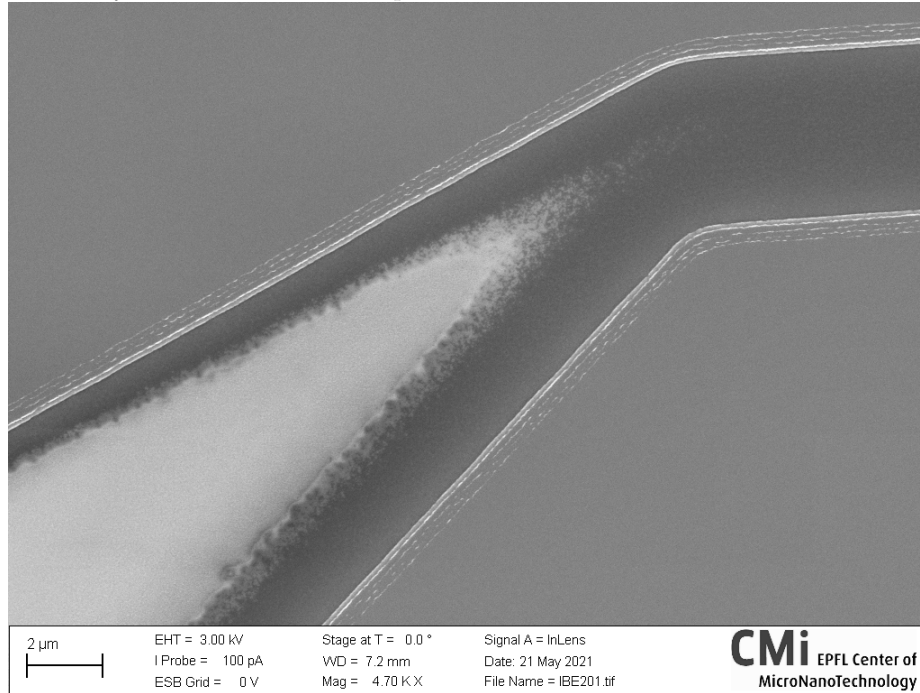
The resist was stripped by putting first the wafer for 30 s in a Tepla GiGAbatch O₂ plasma stripper [72] in the high power regime (600 W power, 400 sccm O₂ flow at 0.8 mbar) in order to remove the top sputtering-damaged layer of resist which is more resilient to wet etching, then putting it 10 minutes in a bath of 1165 remover at 70°C for removing the bulk of the resist and again for 30 s in the Tepla plasma stripper in the low power regime (200 W power, 200 sccm O₂ flow at 0.5 mbar) to clean the potential remains.

3.3.4 Challenges encountered

Some challenges have been encountered during this fabrication process. The first one has been fencing during the ion beam etching, as shown in fig. 19. Fencing is the re-deposition of metal on the sidewalls, which leads to a collapsed 3-dimensional structure that may alter the waveguide properties in an unexpected way. This was caused by the interfacing of a paper sheet between the hotplate and the wafer during the reflow, and removing it made the reflow effective.

The second one has been the non uniform etch rate. Indeed, it has been observed that wide open surfaces were etched at a higher rate than narrow gaps, probably because higher re-deposition or electrostatic charging effects take place in trenches. For completely etched wide open areas, different materials seemed to appear in the trenches (fig. 18). Upon additional etching, the central material

Figure 18: Tapered gap, obtained after 7 minute of low power IBE etching on a 150 nm NbTi coated Si wetox wafer. We can see that a central material (SiO_2) thins as the gap lateral dimension shrinks, showing different dynamics between wide open and narrow areas.



region expanded, indicating that it is the substrate material. This led us to abandon wide open area endpoint detectors in favor of trench endpoint detectors (large arrays of alternating lines and gaps with a width equal to the critical dimension of the design). However the total exposed area was not sufficient to detect the endpoint signal. Even though after 7 minutes of etching with low power there was still some metal remaining, no bi-material pattern in the gap was observed for 10 min of etching, so the trench etch rate is at least 15 nm/min, and at most 25nm/min. Putting more etching time is not a problem since the sapphire etch rate has been reported by CMi staff to be as low as 6 nm/min.

The third one has been the post-coating soft bake of the photoresist on sapphire wafers. This step is part of the automated coating process which is standard on the ACS200 machine, and therefore optimized for Si wafers. The goal is to evaporate the solvent from the resist, and a failure to do it correctly translated in dark erosion of the resist during the development, that is, abnormal stripping of unexposed areas and widening of trenches. This happened because sapphire had a different thermal conductivity and infrared absorption power than Si, so the wafer surface baking temperature was not the one expected. This issue was solved by creating a new recipe with a 10°C higher bake temperature.

The last challenge is linked to an abnormal periodic under-development of certain areas of the wafer. An optical image and a height map of the underdevelopment pattern can be seen in fig. 20. The periodic pattern is explained by the field size of the exposure tool. Indeed, the laser beam profile does not show a constant power along its cross-section. This leads to a lower exposure dose on the rightmost pixels of the field, which is visible as a discontinuity at the point of field stitching. This imperfection in the machine was beyond the possibility of being fixed during this thesis. A similar pattern was found on the dose tests on Si wafers when the dose was too low, however it seems to arise at random localized spots on sapphire wafers, independently of the dose used. Since the NbTi reflective surface is the same as for Si wafers, we believe this issue is another aspect of a baking problem, that is yet to be solved without replacing the expensive optics of the exposure tool.

Therefore, ion beam etching is not yet a usable process, and solving the last stitching challenge is desirable since this method is chemistry independent and will allow to etch other materials such as NbTiN or other metals without the need to optimize a plasma chemistry for it.

3.4 Plasma etching process

This section will present the workflow of the plasma etching process.

Figure 19: IBE reflow comparison. Left : Coupler structure with poor resist reflow (125°C, paper below). This leads to fencing on the edges. Non-uniform trench etching can be observed (not linked to reflow). Right : Coupler structure with good resist reflow (125°C, direct contact with hot plate). Fencing disappeared, we can instead observe inclined edges.

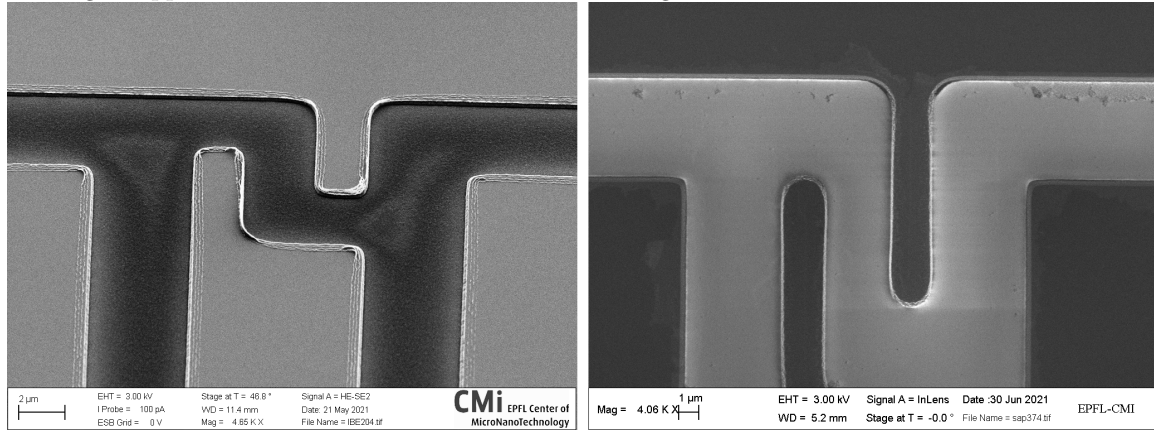
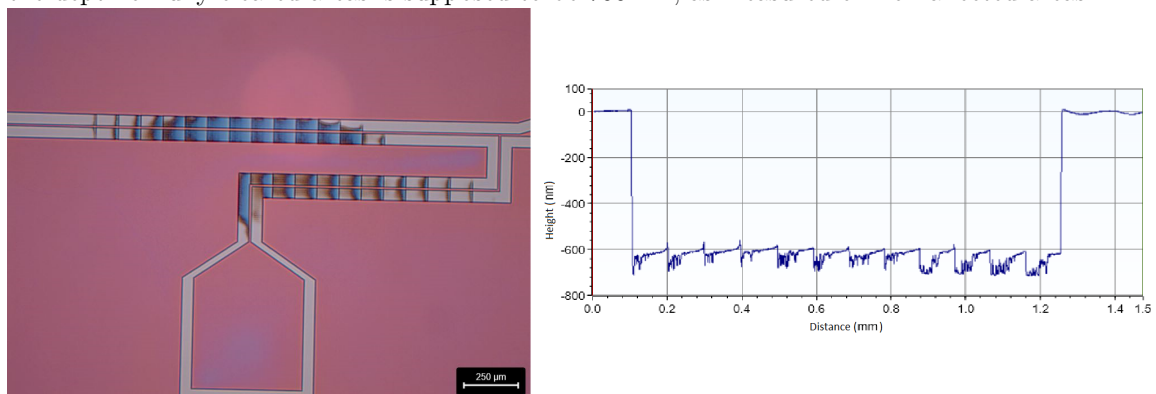


Figure 20: IBE underdevelopment pattern. Left : Optical microscope example of the periodic underdevelopment pattern before etching. Pink is the resist, white is the metal. Right : Mechanical profilometer measurement of the underdevelopment pattern (on a larger structure). For comparison, the depth of fully cleared areas is supposed to be 700 nm, as measured on non affected areas.



3.4.1 Deposition

The deposition step for this process is very similar to the one of the ion beam etching process. It just requires to add a deposition step for a 100 nm layer of Al on the backside of the wafer prior to the NbTi on the front side, because the plasma etching machine used requires a conductive backside surface for electrostatic clamping. The wafer holder has been cleaned with isopropanol to avoid front side contamination, then so has been the front side before NbTi deposition. Sputtering deposition machine and parameters are the same as for NbTi, but the DC power was 400W. Al showed good adhesion to sapphire (AlO_3).

3.4.2 Photolithography

The coating step starts with a thermal dehydration on the ACS200 spin-coater, followed by the spin-coating of 1.5 μm of the positive tone resist AZ ECI3007 (rotation speed : 850 RPM). This resist has been chosen because it is optimized for achieving high resolutions with dry etching processes, enabling us to achieve narrower features in our design. The resist was then soft baked at 110°C for 2 min.

The exposure was done using a 355 nm laser on the VPG200 [73] direct writing exposure tool. This tool is the optical direct writer having the best achievable resolution. A dose of 129 mJ/cm^2 and a defocus of -30% were used. The laser and the defocus are the ones recommended for the resist and the optimal dose has been determined by a dose calibration wafer.

Prior to the development, a post exposure bake of 1 min at 110°C has been done on the ACS200 developing station. The development was performed next using the AZ 726 MIF developer, which is an organic solution based on TMAH. It was followed by a 30 s O_2 low power plasma descumming step on the Tepla stripper in order to remove any resist remaining in the cleared areas and work on a clean surface for the etching.

3.4.3 Etching and resist stripping

The etching was performed on the SPTS APS dielectric etcher [74] which is an ICP based plasma etcher. We have used a CHF_3 and SF_6 plasma for 5 minutes. Unfortunately, the detailed process parameters cannot be disclosed here due to confidentiality reasons. This chemistry is intended for Si_3N_4 etching, but the CMi staff reported using it successfully for Nb etching. It turned out after our tests that it also works for stoichiometric NbTi. The substrate is maintained at room temperature thanks to a backside helium cooling system at 10°C. The endpoint detection system looks for reaction byproducts by optical spectroscopy, however our trench endpoint detection area was not sufficiently large to provide a detectable signal. Independent tests were conducted to determine the etch rate, which has been found to be 29 nm/min after the first minute of etching. The measured etch depth versus time is plotted in fig. 21. In fact, fluorocarbon etching did not show a linear etch rate, as test wafers first etched for one minute showed an etch rate of 55 nm/min. This is explained by the deposition of a thin fluorocarbon layer on the target sample that hinders etching [75]. This film may bring additional losses to our device.

The stripping process has been done in the same sequence as for the ion beam etching process stripping, and then an additional sequence was added because the first one was insufficient, as can be seen by the remaining of a photoresist layer on the metal lines in fig. 22. This additional sequence is a 30 s dip in a bath of HF1%, 15 additional minutes in the 1165 remover bath at 70°C with sonication and finally 1 min of high power O_2 plasma with the Tepla stripper.

3.4.4 Challenges encountered

As in the case of the IBE process, the soft baking of the photoresist during coating was affected by the bad thermal conduction of the Sapphire, with the effect of widening of the exposed features due to dark erosion. This was mitigated by increasing the temperature of the soft bake by 10°C.

Then, the stripping of the thin film was initially performed by a standard plasma-remover-plasma process. However, SEM images revealed a remaining membrane of unknown material deposited over the superconductor, as can be seen in fig. 22 (left). This is due to the fact that fluorocarbon chemistries used for the etching tend to create a chemically cross-linked fluoridated crust at the surface of the resist, making it chemically inert when facing standard removing products [76]. Fluoride ions, such as those found in HF solutions are thought to be effective at attacking the interface between the crust and the metal and resist, thus enabling further lift-off removal. This is shown in the middle panel of fig. 22 and in the right panel after sonication and plasma. It is not clear if the

Figure 21: SPTS etched depth against time. The film was stoichiometric NbTi in all tests conducted. The tests were done by etching and doing profilometric measurements with a mechanical profilometer. The etch rate of the photoresist was monitored independently using a Kapton stencil mask in blank areas, in order to retrieve the metal sheet etch rate from the observed depth variation.

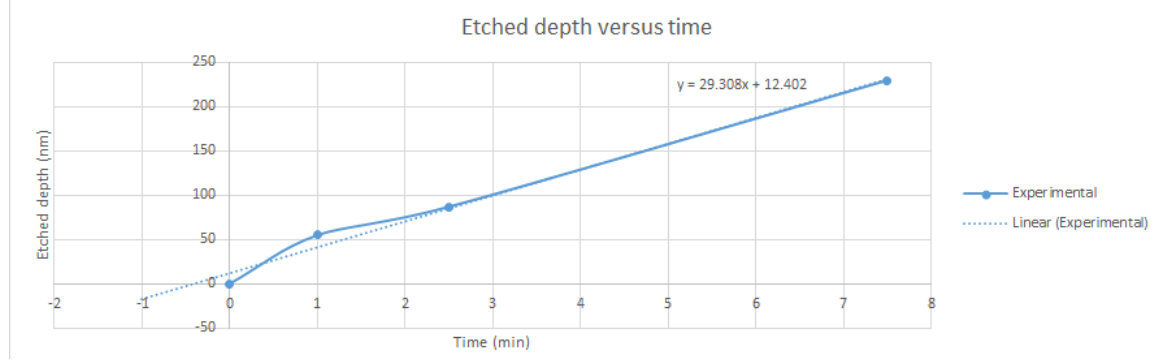
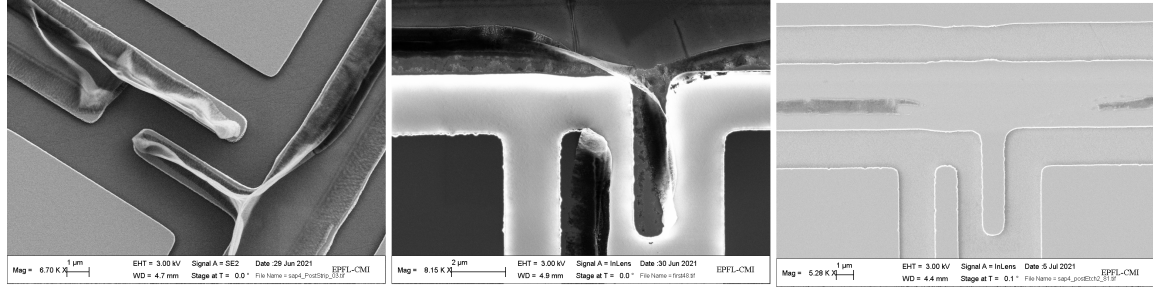


Figure 22: Left : SEM image of the coupler structure after ineffective O_2 plasma and remover stripping. Middle : Same structure after an additional 30 s HF1% dip. Right : Same structure after an additional 15 min dip in remover (sonication for 5 min) at 70°C + 1 min high power O_2 plasma.



first plasma - remover - plasma sequence had any effect at all, and a future wafer made with this process will be tried without. While the HF solution dissolved the Al backside coating, we found that the height step from substrate to the film top changed by less than 5 nm (within the noise of the profilometer height measurement). Energy dispersive X-Ray (EDX) analysis did not show traces of remaining fluor. However, this result is per se not conclusive, since we were searching for the elements in a very thin layer. The EDX volume of interaction on the layer being so small, it may be hard to distinguish the signal from the background noise. However, as shown by the SEM images in fig. 22, most of the remaining fluorinated resist has been etched away.

3.5 Lift-off process

This section will present the lift-off process.

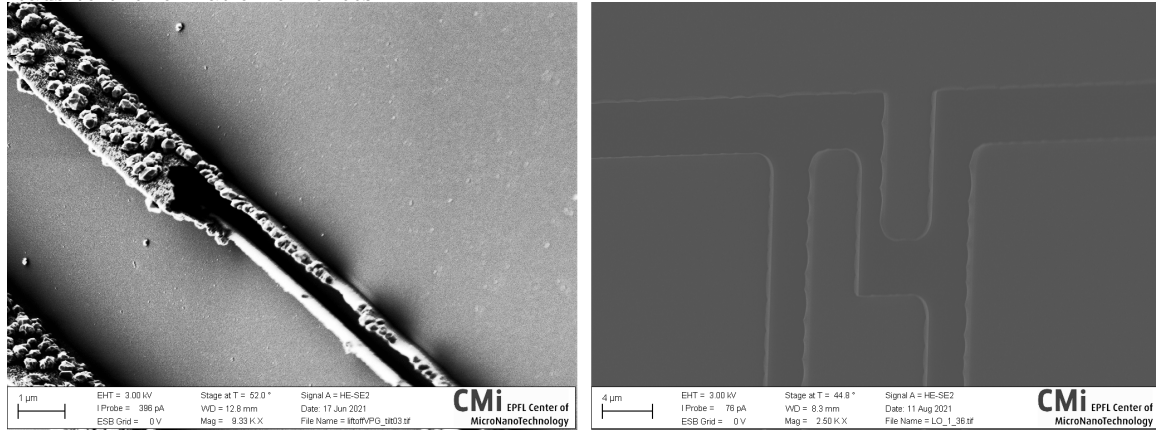
3.5.1 Photolithography

The wafer was first thermally dehydrated on the automatic coater EVG150 [77] before coating a bi-layer resist stack of 400 nm of LOR 5A (lift-off resist, not photosensitive) and 1.1 μm of AZ 1512 HS (photosensitive with positive tone). This has been achieved with rotation speeds of respectively 5650 RPM and 6000 RPM. Each step has undergone a thermal curing after coating, the LOR at 190°C for 250 s and the AZ 1512 at 100°C for 90 s. This photoresist stack was chosen because it allows the most efficient lift-off.

Exposure was done using a 405 nm light source on the MLA150 machine with -2% defocus, as suggested for standard process on this resist. The optimal dose was determined to be $90 \text{ mJ}/\text{cm}^2$ on a Si wafer (the method has not been tried on sapphire). The design has been previously inverted to match the lift-off technique.

Development was made on the same machine as for the coating (EVG150), with the specific developer of the standard recipe, that is AZ 726 MIF as for the dry etching. While the developer chemical is selective on the photoresist, between the exposed and non-exposed regions, the LOR is always dissolved by this product. This leads to a complete opening of the double stack down to

Figure 23: Comparison of lift off processes for two superconducting film thicknesses. Left : 150 nm NbTi film, leads to the formation of small stones and micro-channels. Right : 50 nm NbTi film, leads to the formation of fences.



substrate level on the exposed areas and an undercut below the AZ 1512 resist on the edges of the exposed areas. This was followed by a post development bake at 100°C for 1 min.

3.5.2 Superconductor deposition

Prior to the deposition step, a 30 s low power O_2 plasma descumming was performed in order to remove any remaining resist film on areas that will be covered by metal.

The deposition took place in the same conditions as for the ion beam process, but the thickness deposited was of 50 nm because too thick films risk forming a bridge with the metal deposited on the resist sidewalls.

3.5.3 Lift off

The lift off process starts with a 5 min sonication in a 1165 remover bath. The goal is to promote the detachment of the resist to facilitate further lift off. Then, the sample was left for 3 days in a 1165 remover bath. Most of the resist was lifted-off after this time, however this is a stochastic process and local unwanted metal spots were observed to remain even after 3 days and a sonication.

3.5.4 Challenges encountered

The main challenge that has been encountered during the lift-off process was sidewall deposition. Indeed, the LOR undercut below the AZ resist is made to prevent the deposited film from making a junction with the AZ resist islands, in which case the resist will serve as a backbone structure for the creation of micro-channels that persist after stripping of the resist, as can be seen in fig 23 (left). This happens because the LOR film thickness is not sufficiently high compared to the film thickness. One solution would be to use higher resist stacks but this will imply losing in lateral resolution. The solution chosen was to decrease the film thickness from 150 nm to 50 nm. The result can be seen in fig 23 (right). No channel micro-structure was observed, instead we simply have small fences. Also the little stones observed on the too thick film sample were not reproduced with a thinner film.

3.6 Critical comparison of the processes

This section will finally review all the processes and compare their performances with respect to the figures of merit defined earlier.

First, comparing the waveguide profiles obtained, we can see that the IBE method shows a very smooth profile, although it has a quite trapezoidal cross-section. Indeed, the reflow of the resist induces a slope on the line side. The sloppy region horizontal projection has been measured to be 110 nm wide on the coupler fingers and 290 nm wide on other parts of the design. Then, the lift-off method has shown some fencing to appear on the line walls. Finally, the plasma etching method seems to provide quite vertical walls, although their roughness is higher than with the other methods.

Figure 24: Comparison of the smallest resolved L resolution test structures. Left : Plasma etching, gap of 650 nm by design. Right : IBE, gap of 1.25 μm by design.

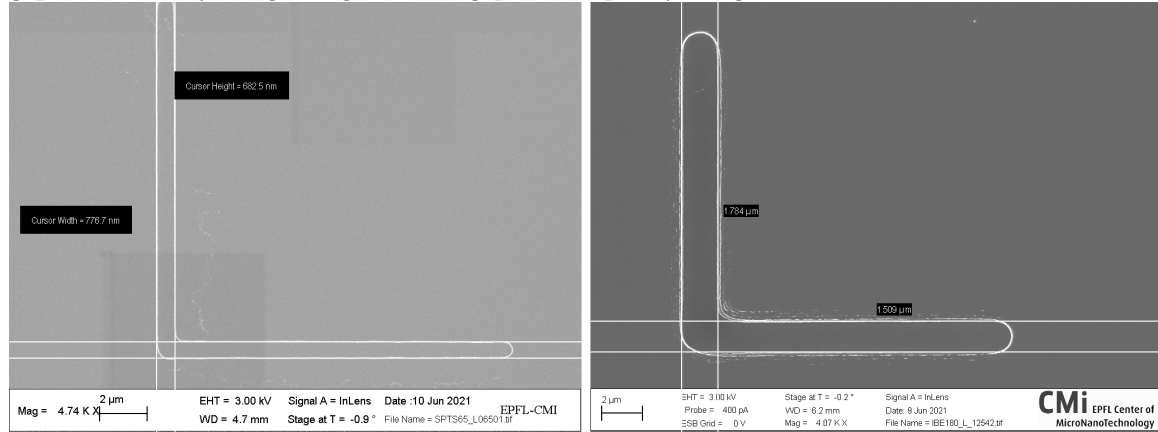
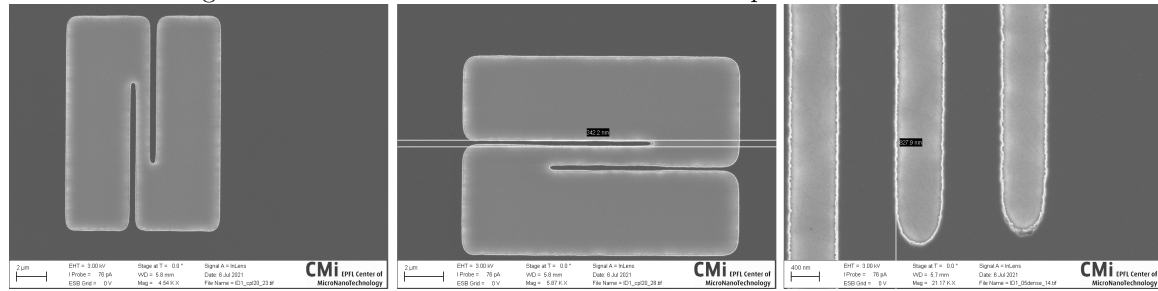


Figure 25: Resolution test structures of the final plasma etched wafer.



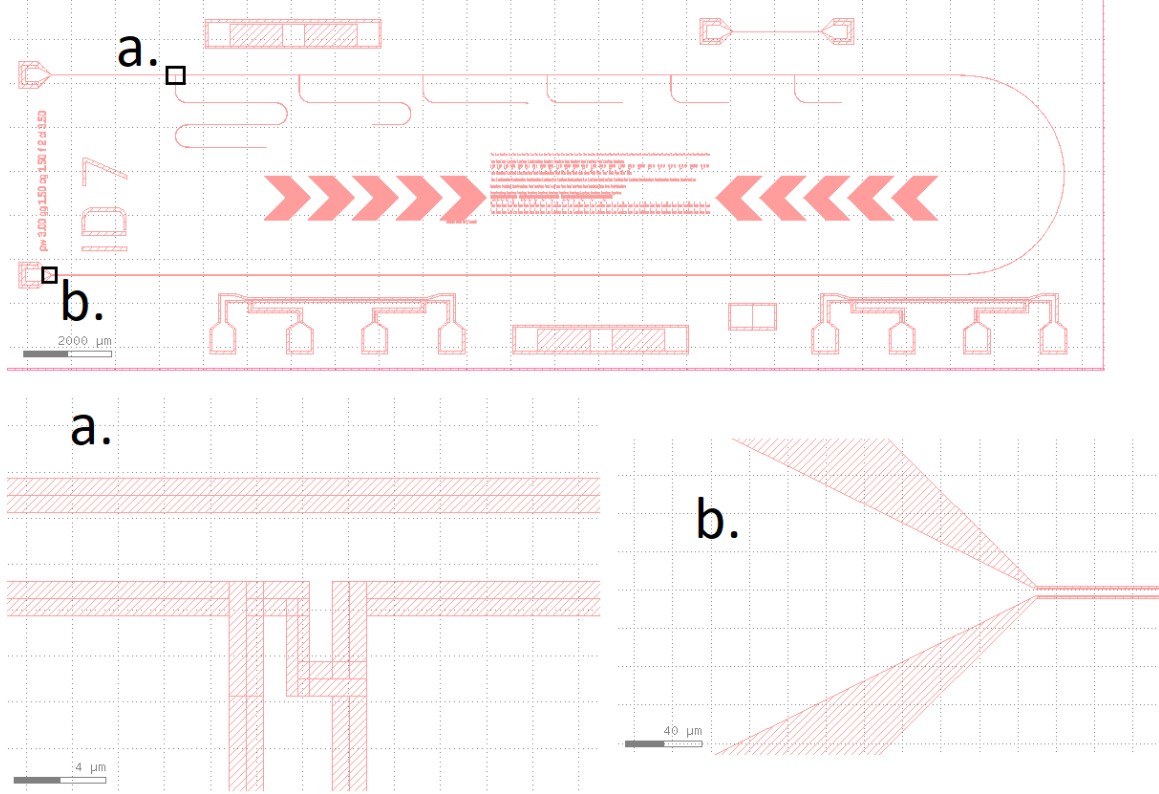
Regarding the faithfulness to the design, the lift-off method has shown poor conservation of the line / gap width ratio, even though the tests have been carried out on wider lines. Maybe it is possible to solve the problem by adapting the design to make the gaps wider. The IBE method is intrinsically limited by the reflow of the resist that blurs out the smallest features like the coupler fingers. Also, this method currently suffers from periodic underdevelopment patterns that make it impractical. The plasma etching method has shown the best pattern resolution with submicron features that were printed. We observe a high faithfulness for features bigger than 1 μm . A comparison of the smallest resolved L resolution test structures of the plasma and IBE methods can be found in fig. 24, where we see that plasma etching resolved a 650 nm gap by design into a 700 nm gap width while IBE did it only for 1.25 μm gap by design resolved into a 1.5 μm gap. A few other test structures from the final wafer (plasma etched) that was diced for cryogenic tests can be found in fig. 25 to illustrate the sub-micron resolution power of the dry etching process flow. We can even observe with the two first panels that resolution is dependent on the scanning direction.

The cost analysis of the methods has been carried out by ignoring the costs related to the wafer purchase, the final dicing and wire bonding to the PCB and the inspection costs (SEM, profilometer, electrical probe station). Obviously, the costs evaluated are noisy because the billing is made as a function of the total machine use time, which is subject to small variations. It has revealed that the IBE method costs 162 CHF for the processing, the plasma etching 210 CHF. The higher price is explained by an additional backside deposition and more etching steps undertaken. However, it may be possible to remove some stripping steps and bring down this price. Finally, the lift-off method costs 162 CHF. Although it makes economy on etching and stripping steps, the bilayer photoresist coating is much more expensive than monolayers for other methods. Therefore, the processing methods are costing about the same amount of money.

Finally, regarding chemical contamination of the film, the lift-off method is expected to be the less prone to modify the surface. IBE may damage the surface by implanting ions and breaking the crystalline structure upon physical sputtering. However, EDX data did not show clear contamination. However, it should be noted that the EDX method samples a large interaction volume, so detecting surface traces may be tough and the signal fall below the noise level. Similarly, the plasma etching method is prone to the deposition of a fluorocarbon film. HF dipping is expected to have cleaned it away, as EDX data did not show any trace of fluor, but again this method has its limits.

As a conclusion, given the results obtained during the fabrication process characterization, we will proceed to fabricate the final sample with the plasma dry etching process. The next section will introduce the final layout adopted as well as content related to the cryogenic characterization of the device.

Figure 26: Final layout of a chip. Red is the substrate, white is the superconductor. a. is a zoom on a coupler. b. is a zoom on the output pad tapering.



4 Realization of a multiple resonator network prototype

We will present here the final layout that was adopted, taking into account theoretical considerations and constraints from the fabrication processes. The layout was designed using the Raith GDSII Matlab Toolbox [78], allowing to create a code generating the different sub-structures in a parametric way. Doing so allows to very quickly generate chips with different parameters on the same wafer.

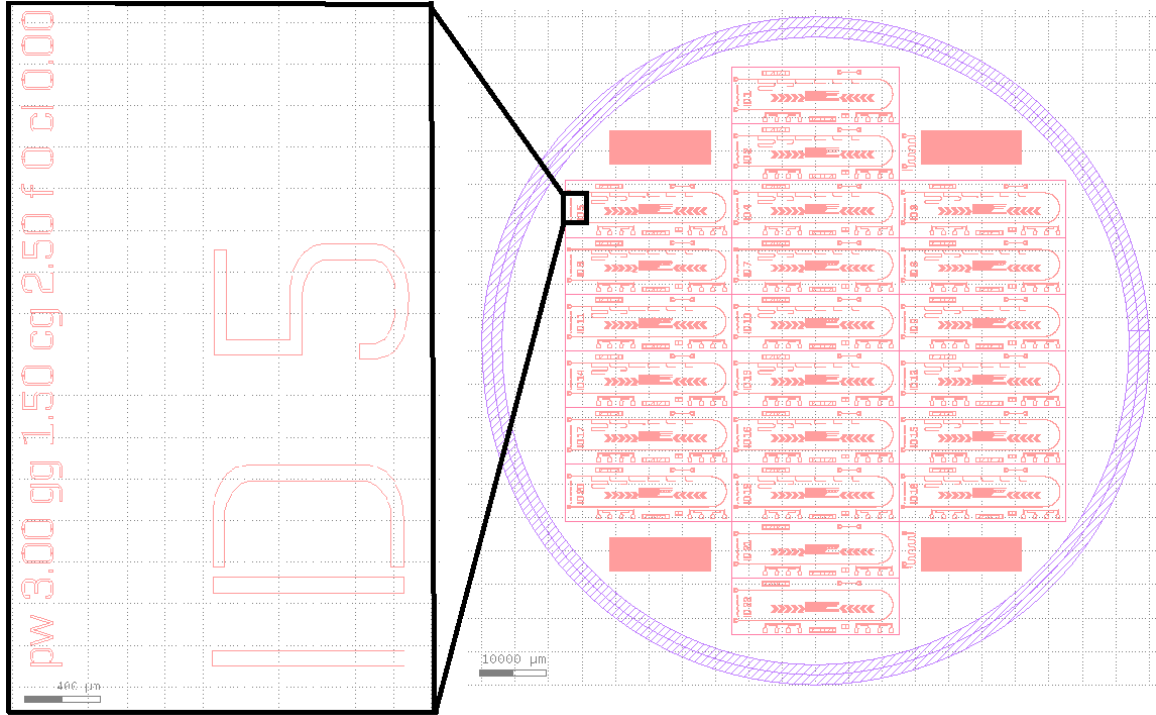
An example of a chip layout can be found in fig. 26. Features have been put $300\text{ }\mu\text{m}$ away from the dicing lines to avoid damaging during the dicing. The distance between the input and output RF pads has been set to match that of the PCB to allow the shortest wire bond length possible. The same argument constrains the bottom test structures with DC pads.

The first resonator has been put at a good distance from the input pad to avoid an unexpectedly high coupling capacitance. Indeed, in coplanar geometries, the capacitance between two lines tends to be conserved when the line width / distance between lines ratio is conserved, and the pad width is about 100 times that of the resonator line width. A similar argument applies for the coupling of the first meander turn to the through line running parallel to it. A sufficient distance has been put to minimize this coupling. The resonance frequencies have been selected to be between 4 and 24 GHz with a step of 4 GHz. It should be noted that these theoretical frequencies do not take into account the coupler and turn contributions and are subject to the approximation errors summarized in table 2.

A schematic of the wafer layout is represented in fig. 27. Using a code that computes the most efficient packing of the chips to fit as much as possible on the wafer, 22 numerated chips could have been fitted. However the top and bottom ones have been damaged during processing due to manipulation with the tweezers. The parameters chosen for each chip are summarized in table 3.

The two bottom ones (number 21 and 22) include very short resonators of a few μm to allow probing the background spectrum of the device unloaded from resonators in the frequency range of interest. The other chips were used to swipe geometrical parameters on a set of resonators of fixed theoretical resonance frequencies. The central line / gap width ratio has been kept constant to have $50\text{ }\Omega$ everywhere, but the central line widths range from $2\text{ }\mu\text{m}$ to $8\text{ }\mu\text{m}$. The couplers have been chosen to be finger couplers for this design, looking the same as in fig. 19. The coupling capacitance

Figure 27: Final layout of the wafer. Red is substrate, white is superconductor and blue is an artificial layer symbolizing the 3mm exclusion zone near the wafer border.



values have been swiped for each line width by varying the fingers length. This allows to have several coupling quality factors and will eventually be helpful in finding the critical coupling point. Finger couplers in this design don't allow to make the through line wider to reduce losses, so it is the same width as the resonators.

Dense line endpoint detection structures can be found in the corners of the wafer and surrounding the resolution test structures on the chips. Dense lines were used instead of wide rectangles because the IBE process showed a lower etch rate for narrow gaps, so the endpoint signal would be more representative of the state of our narrow features.

Now that the final layout has been introduced, the next sections will present the electrical readout scheme and the cryogenic setup.

Cell ID	Central line width (μm)	Coupler type	Coupler dimension (μm)	C_c (fF)	Comments
1	2	gap	2	0.12	Damaged
2	2	gap	4	0.05	
3	2	finger	2	0.23	
4	2	finger	6	0.4	
5	3	gap	2.5	0.18	
6	3	gap	5	0.08	
7	3	finger	3.5	0.33	
8	3	finger	9.5	0.61	
9	4	gap	3	0.25	
10	4	gap	6	0.1	
11	4	finger	4	0.39	
12	4	finger	13	0.77	Damaged
13	5	gap	3.5	0.3	
14	5	gap	7	0.12	
15	5	finger	5.5	0.48	
16	5	finger	16.5	0.96	Damaged
17	8	gap	4.5	0.48	
18	8	gap	9	0.19	
19	8	finger	11	0.76	Damaged
20	8	finger	28	1.5	
21	2	finger	6	0.4	Background spectrum acquisition
22	4	finger	6	0.44	Background spectrum acquisition, damaged

Table 3: Table of the final layout chips theoretical properties. The coupler dimension is the finger length for the finger coupler and the coupling gap width for the gap coupler. C_c is the coupling capacitor.

5 Cryogenic characterization of the devices

This last part will present the results of the cryogenic experiments on the devices. It will start by presenting the electronic readout scheme and the cryogenic setup. Then, experiment results will be introduced, followed by a discussion of and interpretation of the results.

5.1 Measurement setup

The measurement setup comprises two main parts. First it is necessary to provide a cold environment for the sample to reach the superconducting state. Second, an electronic RF setup is needed to power the resonators and characterize their response. In the next paragraphs these two systems will be presented.

5.1.1 Cryogenic system

We were initially planning to use a cryogenic station that allows to control the temperature inside in order to measure the resonance frequency shift versus temperature. Unfortunately, due to unexpected failure in previous experiments performed on this facility, the setup could not be available in the time frame of this thesis.

Alternatively, a liquid helium Dewar was available. This allowed to perform measurements by submerging the chip directly into the liquid helium, which provides a stable temperature environment of 4.2 K. A picture of the system can be found in fig. 28. The helium level was sufficient to make our sample superconductive and conduct several tests. However, with such a system we had no control over the temperature, so no temperature data could be measured.

5.1.2 Electronic instrumentation

The flange available to mount the chip inside the Dewar had only one RF channel available. For this reason, although our design was intended for transmission measurements, the measurements were

Figure 28: Photo of the cryogenic system. In the center : the Dewar with on top an RF cable exiting from the flange.



Figure 29: Photo of the final chip.

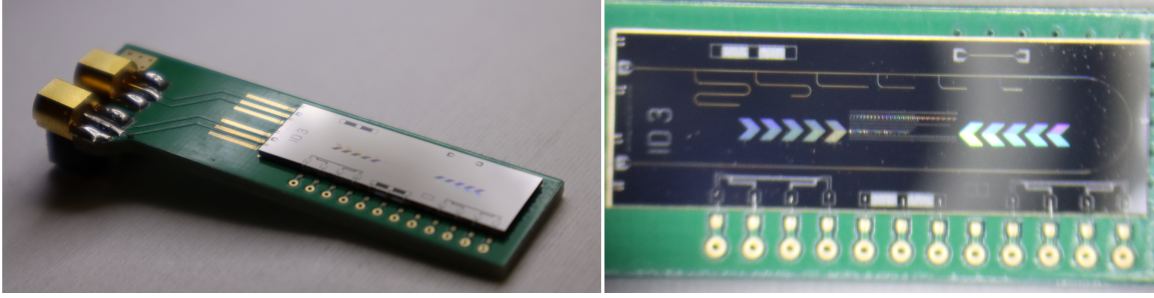
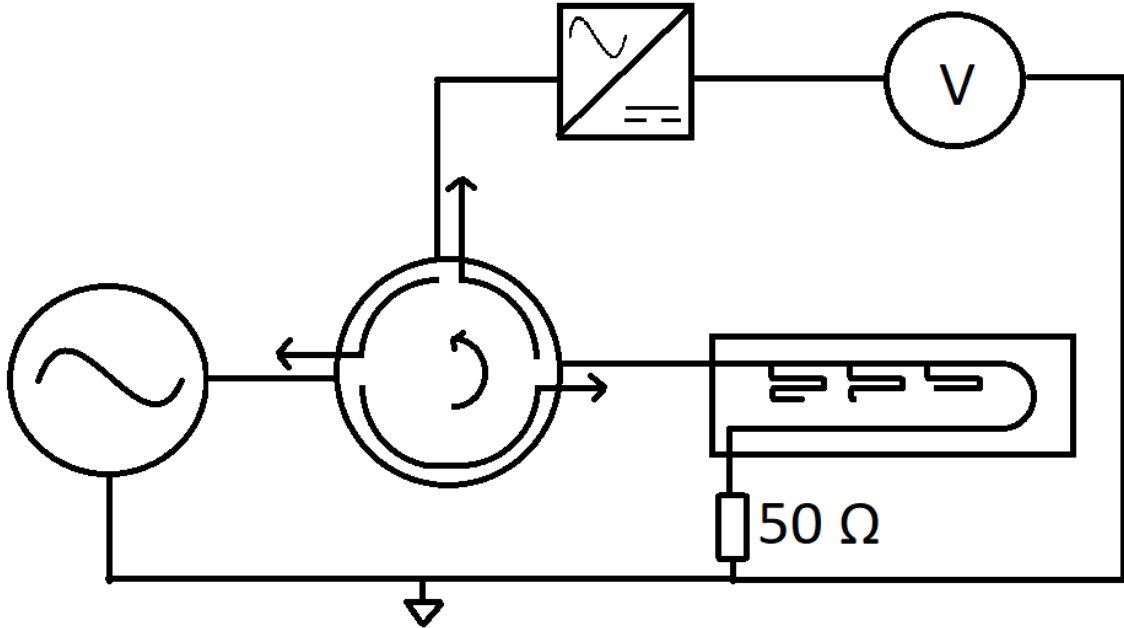


Figure 30: Schematic of the electronic setup.



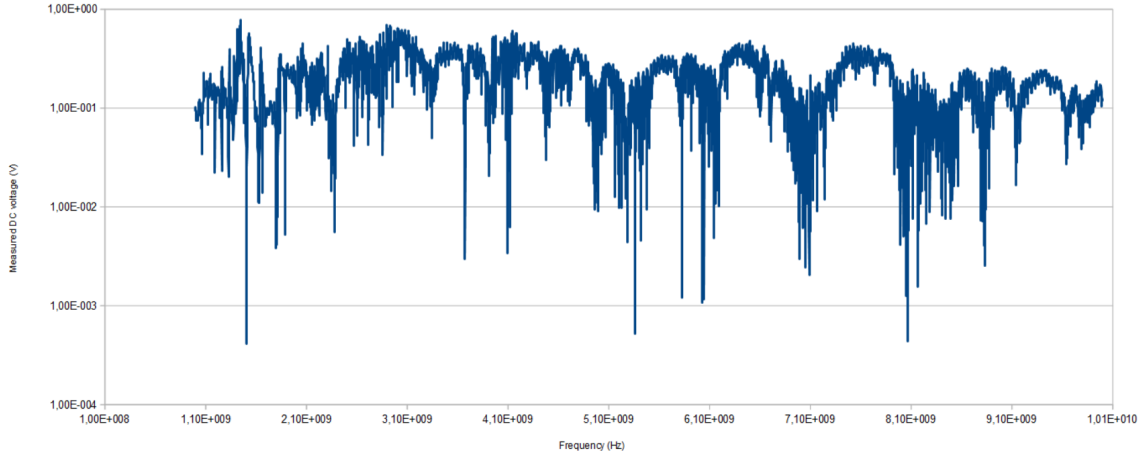
performed in reflection on the input channel. The output channel has been terminated by soldering a $50\ \Omega$ resistor between the output signal line and the ground plane. In this way the output of the through line is a matched $50\ \Omega$ port and we should observe only the reflections due to the resonators (plus those of the imperfect RF network).

A schematic of the electronic setup can be found in fig. 30. A local oscillator (LO) swipes a frequency range from 1 GHz to 10 GHz with a step size of 1 MHz and an integration time of 100 ms. The power level used is 20 dBm. A circulator ensures that the forward and backward signal are routed correctly, the forward being sent to the chip and the backward to the detector setup. The detector setup consists of a rectifier diode bridge that operates an AC to DC conversion. The DC signal voltage is then read out. A photo of the final chip mounted on its PCB is shown in fig. 29. The PCB simply routes the AC signal from the chip ports to the PCB ports. Other ports for DC measurements were put on, however these have not been used in this study.

Only one chip has been selected for this study, that is the chip with ID 20, with a $8\ \mu\text{m}$ central line width and a $1.5\ \text{fF}$ coupler capacitor. We chose this chip because we expect it to have less losses than the others because of its central line width, and has the highest coupling capacitor. It should therefore be the closest to the overcoupled regime and benefit from a low insertion loss. This is critical since we do not have an amplifier in our setup, so undercoupled samples may have shown too shallow resonances to be detected.

Now that the experimental setup has been introduced, the next section will present the experimental results.

Figure 31: Measured spectrum (DC voltage on detector) of the chip + electronic setup. Integration time of 100 ms with a source power of 20 dBm and step of 1 MHz.



5.2 Experimental data obtained

This section will present all the studies conducted on our sample and their results. We will start by a measure outside of the cryostat to measure the film resistivity, then the RF measurements using the system described in the previous section will be introduced and finally a study of the critical current density has been carried out.

We have first measured the resistivity of the NbTi film at room temperature using a four wire measurement technique. The four-probe structure in fig. 16 has been used for this purpose. The outermost pads served as current source and ground, the innermost pads were connected to voltmeters. Knowing the current flowing and the voltage across a section of conductor, we are able to derive its resistance. Then, from its geometry (width : $9.95 \mu\text{m}$ with SEM, thickness : $0.15 \mu\text{m}$ with mechanical profilometer and length of $3935 \mu\text{m}$ from design), we compute its resistivity. We obtained a resistivity of $8.8 \times 10^{-7} \Omega\cdot\text{m}$.

Then, we know that the chip was superconducting by doing a preliminary DC resistance measurement from the flange of the cryostat down to the chip and the output resistor with a multi-meter. A value of 49.7Ω has been measured. Since the superconducting chip is supposed to have zero DC resistance, the RF cables a low one, and the termination resistor 50Ω at room temperature, we can conclude that the chip is indeed superconducting. For the record, the same measurement at room temperature yielded about $180 \text{ k}\Omega$.

Using the cryostat and the RF setup we have made an RF reflection measurement on the chip. The DC voltage measured by the detector versus frequency can be found in fig. 31.

Finally, a last study consisted in finding the critical current density of the NbTi film. In order to do so, a DC voltage source was connected to the flange of the cryostat and connected to the chip. We observe the current associated with the voltage applied. We observed a linear increase of the current with the voltage corresponding to the 50Ω of the resistor, and when a value of approximately 40 mA (2 V) is reached, the current falls to 2 mA . This value remains approximately stable upon voltage increase and decrease down to 0.1 V (2 mA). Therefore, the critical current is about 40 mA .

5.3 Discussion of the results

The room temperature resistivity of NbTi obtained ($8.8 \times 10^{-7} \Omega\cdot\text{m}$) is of the same order as values reported in the literature [79], where they found a value of approximately $8 \times 10^{-7} \Omega\cdot\text{m}$ for stoichiometric NbTi at 250K .

Looking at the spectrum in fig. 31, we can difficultly obtain any information about our chip from the measured signal, for several reasons. First, it is possible that our transmission line is not at 50Ω due to the effects of kinetic inductance. Indeed, it has been estimated in section 2.4.2 that the characteristic impedance was under-estimated by about 10% . This would lead to mismatches with the RF cables and the termination resistor, ending up with parasitic reflections, that add up with those of the RF cable and electronics. Indeed, the longer the cables and the more cable connections

there are, the more parasitic reflections there are. Our RF cable setup was not optimal on this matter because due to a lack of appropriate cables we needed to use SMA to SMP cable connectors. Therefore, identifying the resonance dip caused by the resonators is a tough task, given the density of resonance dips found in the spectrum. Furthermore, for the same reasons the characteristic impedance was under-estimated, the resonance frequencies were over-estimated by 7.7 % to 16.7 %, so there is little information about which part of the spectrum to look at to find the resonance dips.

This first RF measurement teaches us a few guidelines about how to improve the setup for the future measurements. First, in order to eliminate the parasitic reflections, we may create for each central line width used a chip without resonators that will give us the background spectrum. Further measurements with chips with resonators will then be facilitated by subtracting the background spectrum. Then, we will use transmission measurements rather than reflection measurements and change the detector system. Indeed, we were measuring here the amplitude of the signal, while a preferred technique would be to measure the phase of the signal using IQ mixers. Our frequency step size was 1 MHz wide, which makes resonators with a Q factor in the order of 1000s detectable on the spectrum. It is possible that our resonators have higher Q factors, and that their resonance dips don't appear on the spectrum for this reason. Switching to phase measurement allows to detect a phase shift by passing through the resonance frequency, so the resonance cannot be missed. Then, once identified, it is possible to refine the frequency step around this frequency. In order to anticipate a problem we may have, we can also try to integrate a HEMT cryogenic amplifier after our chip. Indeed, we don't know before the measurement if we are undercoupled or overcoupled, so if the insertion loss is high (over-coupling), we may not see the resonance peak as it will be shallow.

Finally, we will discuss the critical current measurement. The fall in measured current from 40 mA to 2 mA is explained by a local transition to the normal state. After the normalization of a region, power will be dissipated resistively, keeping the region in the normal state even upon diminution of the applied voltage. The only way to make the region superconductive again is to decrease sufficiently the voltage so that the heat generated by ohmic losses is lower than the heat exchanged with the medium. A stable current upon voltage increase after transition to normal state means that the resistance is linearly increasing. This may be explained by the expansion of the normal region upon application of higher voltages. Finally, assuming that the current density inside the superconducting line is constant, which is justified by the fact that the thickness of the line (150 nm) is smaller than $2\lambda_L$, we have a critical current density of 33 kA / mm² (line thickness is 8 μ m). This compares with CERN data about NbTi strands [80] where they found for 100 mT of applied field and at 4.2 K a critical current density of about 30 kA / mm². We therefore expect that the power level used for the RF measurements was not high enough to make the sample non superconductive (The current is fixed by the 50 Ω resistor, and 20 dBm = 2.5 V RMS, but the RF cables produce many reflections so the voltage at the chip level should be lower).

6 Conclusion

The goal of this project has been set to produce a distributed cryogenic temperature sensor that uses as few cables as possible and that is competitive with the state of the art in minimal cabling cryo temperature sensing. More specifically, for the first milestone of the project that is represented by this thesis work, we aimed to optimize the MKID design parameters for our specific purpose, develop fabrication methods allowing us to reach conditions as close as possible to the theoretical ones, and test the RF and superconducting properties of a final sample.

To do so, a first bibliographical research has been done in order to understand the superconductor and RF engineering theories and identify the relevant parameters for temperature sensing. Also, a state of the art literature review of MKID technology allowed us to identify the best practices while optimizing some design parameters for our application. We have kept from the MKID literature the idea of aiming at low film thicknesses and narrow lateral dimensions to increase sensitivity. Furthermore, we emphasized the need to take into account the widening of the effective gap seen by the magnetic field due to the London penetration depth, that is not taken into account in most state of the art MKID papers. Indeed, as lateral dimensions become smaller, and as our application works closer to the critical temperature, this effect may become significant. The RF engineering concerns were the same as photo-sensing MKIDs. However, we needed to take into account our specific application when choosing the materials. Indeed, most authors are not concerned by the temperature variation of the substrate properties since they don't aim to measure the temperature. Also, since we don't aim at measuring transient absorption events, we pointed out that making full NbTiN MKIDs was a great idea for temperature sensing, while for photo-sensing this would not allow the quasiparticles to survive long enough to be detected.

Then, we investigated three fabrication methods (IBE, plasma etching and lift-off) with respect to a few figures of merit, that are reaching the smallest lateral dimensions, being low cost, having a rectangular waveguide profile and avoiding chemical contamination. A few challenges needed to be solved to get a usable result, which were unfortunately not entirely solved for the IBE case. It turned out that all the methods were equivalent in terms of cost, and no contamination was detected, up to the poor accuracy of the EDX method for probing a thin surface layer. Regarding achievable resolution and waveguide profile, it turned out that the plasma etching method was the most suitable, so it has been decided to select it as the production method. Indeed, with plasma etching we have been able to reach the resolution limits of optical lithography, down to about 650 nm in lateral dimensions with a typical error of 50 nm with respect to the design.

Then, a Matlab code was written to automatize the layout generation with design parameters in input. The code allowed to find an optimal packing of the chips on the wafer for their given dimensions and to swipe parameters across all the chips. A final design corresponding to our requirement has then been produced, diced and wire-bonded to the PCB chip.

Finally, a few experimental studies have been carried out. We measured the resistivity of the film and found values close to that of the literature. We also measured a critical current density close to that of the literature in comparable temperature and field regimes. This validated the quality of our film. We also tried to perform a reflection RF measurement of our chip in an helium Dewar due to lack of hardware. This has not been conclusive as we have not been able to identify the resonance dips. However, this has taught us valuable insights about how to improve the setup.

In order to reach the first milestone of the project, that is getting an RF spectrum where we can clearly identify the resonance frequencies and observe their shift with respect to temperature, there is still some further work to be done. First, by improving the measurement setup. Indeed, using phase measurements rather than amplitude measurements will allow to detect high Q resonators even when the frequency step is too large. Building a transmission setup with higher quality cables will also reduce the parasitic reflections, and using specific chips without resonators to acquire the background spectrum will allow to subtract it from further resonator measurements.

Then, further studies can be conducted in the fabrication processes. Indeed, we may try to remove the first resist stripping sequence from the plasma etching process flow as it is ineffective. Then, the IBE method still requires to solve the periodic underdevelopment pattern that prevents it from currently working. This is important because IBE will allow to quickly make samples with other superconductors without developing new plasma etching methods. NbTiN is especially an interesting target given its theoretical properties.

Finally, studies of samples with different design parameters are left to be done. Investigating the properties of thinner superconductor films may lead to a dramatic enhancement of the temperature

sensitivity. Bi-section resonator designs may allow to reduce the dielectric losses. Trying other coupler types and finding the critical coupling condition will allow to obtain the best trade off between insertion loss and Q factor.

To conclude, even if some work needs to be done to reach the first milestone, the work of this thesis has allowed a good starting point for the project with a working process flow, a code for generating designs and a bibliographic and theoretical analysis leaving room for future studies.

References

- [1] A.V. Matheoud et al. A single chip electron spin resonance detector based on a single high electron mobility transistor. *Journal of magnetic resonance*, 294, 2018.
- [2] A.V. Matheoud et al. A low-power microwave hemt lc oscillator operating down to 1.4 k. *IEEE TRANSACTIONS ON MICROWAVE THEORY AND TECHNIQUES*, 67, 2019.
- [3] PK Day et al. A broadband superconducting detector suitable for use in large arrays. *Nature*, 425, 2003.
- [4] Superconductor phase diagram. <http://hyperphysics.phy-astr.gsu.edu/hbase/Solids/solref.html#hlf>. Accessed: aug 2021.
- [5] H.J. Herman. The superconducting magnet system for the atlas detector at cern. *IEEE transactions on applied superconductivity*, 10, 2000.
- [6] N. Mitchell et al. The iter magnet system. *IEEE transactions on applied superconductivity*, 18, 2008.
- [7] S. Yokoyama et al. Research and development of the high stable magnetic field rebco coil system fundamental technology for mri. *IEEE transactions on applied superconductivity*, 27, 2017.
- [8] S. Honjo et al. Status of superconducting cable demonstration project in japan. *IEEE transactions on applied superconductivity*, 21, 2010.
- [9] K Rajashekara et al. A review of cryogenic power electronics - status and applications. *Workshop on Accelerator Magnet, Superconductor, Design and Optimization*, 2013.
- [10] HL Huang et al. Superconducting quantum computing: a review. *Sci. China Inf. Sci.*, 63, 2020.
- [11] V. Parma. Cryostat design. *CAS - CERN Accelerator School: Superconductivity for Accelerators*, 2013.
- [12] J. Schwartz. Quench in high temperature superconductor magnets. *Workshop on Accelerator Magnet, Superconductor, Design and Optimization*, 2013.
- [13] Z. Zhang et al. Experimental study on temperature control method for the thermal cycling tests of a superconducting magnet mock-up. *IEEE Transactions on applied superconductivity*, 2020.
- [14] S. Pamidi et al. Cryogenic helium gas circulation system for advanced characterization of superconducting cables and other devices. *Cryogenics*, 52, 2012.
- [15] C.J. Yeager et al. A review of cryogenic thermometry and common temperature sensors. *IEEE sensors journal*, 1, 2001.
- [16] R.L. Rusby et al. Cryogenic temperature measurement. *Revue générale de thermique*, 35, 1996.
- [17] V. De Cosmo et al. Carbon composition resistors for cryogenic thermometry. *Review of scientific instruments*, 58, 1987.
- [18] T. Yotsuya et al. New type cryogenic thermometer using sputtered zr-n films. *Applied Physics Letters*, 51, 1987.
- [19] S. Scott Courts et al. Review of cernoxTM (zirconium oxy-nitride) thin-film resistance temperature sensors. *AIP Conference Proceedings*, 684, 2003.
- [20] J. Nelson et al. Thin film cryogenic thermometers defined with optical lithography for thermomagnetic measurements on films. *Review of scientific instruments*, 86, 2015.
- [21] M. Bose et al. Study of forward characteristics of a cryogenic temperature sensor diode. *Review of Scientific Instruments*, 67, 1996.
- [22] B. Okcan et al. A cryogenic analog to digital converter operating from 300 k down to 4.4 k. *Review of Scientific Instruments*, 81, 2010.

- [23] M. Turqueti et al. Deep cryogenic low power 24 bits analog to digital converter with active reverse cryostat. *Physics Procedia*, 67, 2015.
- [24] S Gupta et al. Fiber bragg grating cryogenic temperature sensors. *Applied Optics*, 35, 1996.
- [25] F. Scurti et al. Quench detection for high temperature superconductor magnets: a novel technique based on rayleigh-backscattering interrogated optical fibers. *Superconducting science and technology*, 29, 2016.
- [26] F. Scurti et al. Optical fiber distributed sensing for high temperature superconductor magnets. *Proceedings of SPIE*, 2017.
- [27] V De Miguel-Soto et al. Study of optical fiber sensors for cryogenic temperature measurements. *Sensors*, 17, 2017.
- [28] S. Ishigami et al. Growth of high quality quartz crystal and its application to temperature sensors. *IEEE INTERNATIONAL FREQUENCY CONTROL SYMPOSIUM*, 1994.
- [29] K. Agatsuma et al. High resolution cryogenic quartz thermometer and application to wireless measurement. *Cryogenics*, 34, 1994.
- [30] N. Tamada et al. Wireless multi-temperature measurement for rotating cryogenic machines. *IEEE TRANSACTIONS ON MAGNETICS*, 28, 1992.
- [31] M. Fukami et al. All-optical cryogenic thermometry based on nv centers in nanodiamonds. *Physical review applied*, 12, 2019.
- [32] B. Mazin. *Microwave Kinetic Inductance Detectors*. PhD thesis, Caltech, 2004.
- [33] A Walter et al. MEC: the MKID exoplanet camera for high contrast astronomy at Subaru (Conference Presentation). In *Ground-based and Airborne Instrumentation for Astronomy VII*, volume 10702. International Society for Optics and Photonics, SPIE, 2018.
- [34] R.M.J Janssen et al. Equivalence of optical and electrical noise equivalent power of hybrid nbtin-al microwave kinetic inductance detectors. 105, 2014.
- [35] R. Barends et al. Niobium and tantalum high q resonators for photon detectors. *IEEE Transactions on Applied Superconductivity*, 17, 2007.
- [36] J.E. Sauvageau and D.G. McDonald. Superconducting kinetic inductance bolometer. *IEEE Transactions on Magnetics*, 25(2):1331–1334, 1989.
- [37] D.G. McDonald. Novel superconducting thermometer for bolometric applications. *Appl. Phys. Lett.*, 50, 1987.
- [38] P. Mangin et al. *Superconductivity, an introduction*. 2017.
- [39] J. Bardeen, L. N. Cooper, and J. R. Schrieffer. Theory of superconductivity. *Phys. Rev.*, 108:1175–1204, Dec 1957.
- [40] F. London and H. London. The electromagnetic equations of the superconductor. *Proc. R. Soc. Lon.*, 149, 1935.
- [41] J. Pearl. Current distribution in superconducting films carrying quantized fluxoids. *Appl. Phys. Lett.*, 5, 1964.
- [42] A.A. Abrikosov. The magnetic properties of superconducting alloys. *Journal of Physics and Chemistry of solids*, 2, 1957.
- [43] Drude model. https://en.wikipedia.org/wiki/Drude_model. Accessed : 2021.
- [44] A.J. Annunziata et al. Tunable superconducting nanoinductors. *Nanotechnology*, 21, 2010.
- [45] J. Gao. *The Physics of Superconducting Microwave Resonators*. PhD thesis, 2008.
- [46] R.M.J Janssen et al. Power handling and responsivity of submicron wide superconducting coplanar waveguide resonators. 167, 2012.

- [47] B.A. Mazin. Superconducting materials for microwave kinetic inductance detectors. *arXiv:2004.14576*, 2020.
- [48] R. Sarpeshkar, T. Delbruck, and C.A. Mead. White noise in mos transistors and resistors. *IEEE Circuits and Devices Magazine*, 9(6):23–29, 1993.
- [49] W.A. Phillips. Tunneling states in amorphous solids. *J Low Temp Phys*, 7, 1972.
- [50] John R. Clem. Inductances and attenuation constant for a thin-film superconducting coplanar waveguide resonator. *Journal of Applied Physics*, 113, 2013.
- [51] R. Barends. *Photon-detecting superconducting resonators*. PhD thesis, 2009.
- [52] A. Gauzzi et al. Very high resolution measurement of the penetration depth of superconductors by a novel single-coil inductance technique. *REVIEW OF SCIENTIFIC INSTRUMENTS*, 71, 2000.
- [53] A.D O’Connell et al. Microwave dielectric loss at single photon energies and millikelvin temperatures. *Appl. Phys. Lett.*, 92, 2008.
- [54] J. Krupka et al. Complex permittivity of some ultralow loss dielectric crystals at cryogenic temperatures. *Meas. Sci. Technol.*, 10, 1999.
- [55] A. Smakula et al. Dielectric properties of semiconductors at low temperatures. *Journal of Applied Physics*, 43, 1971.
- [56] D.M. Pozar. *Microwave Engineering*. 2005.
- [57] Transmission line theory. https://en.wikipedia.org/wiki/Transmission_line/.
- [58] Simons Rainee N. *Coplanar Waveguide Circuits, Components and Systems*. Wiley-Interscience, 2001.
- [59] Zeev nehari. *Conformal Mapping*. 1952.
- [60] Coplanar waveguide calculator. <http://wcalc.sourceforge.net/cgi-bin/coplanar.cgi>. Accessed: 2021.
- [61] M. Göppl et al. Coplanar waveguide resonators for circuit quantum electrodynamics. *J App Phys*, 104, 2008.
- [62] G.E. Ponchak et al. Excitation of coupled slotline mode in finite-ground cpw with unequal ground-plane widths. *IEEE TRANSACTIONS ON MICROWAVE THEORY AND TECHNIQUES*, 53, 2005.
- [63] J. Lee et al. Suppression of coupled-slotline mode on cpw using air-bridges measured by picosecond photoconductive sampling. *IEEE MICROWAVE AND GUIDED WAVE LETTERS*, 9, 1999.
- [64] S. Wilde et al. Physical vapour deposition of nbtin thin films for superconducting rf cavities. *proceedings of IPAC2017*, 2017.
- [65] Soft bake by microchemicals. https://www.microchemicals.com/technical_information/softbake_photoresist.pdf.
- [66] Post-exposure bake by microchemicals. https://www.microchemicals.com/technical_information/photoresist_post_e.
- [67] Hard bake by microchemicals. https://www.microchemicals.com/technical_information/hardbake_photoresist.pdf.
- [68] Dp650 machine. <https://www.epfl.ch/research/facilities/cmi/equipment/thin-films/alliance-concept-dp-650/>.
- [69] Acs200 machine. <https://www.epfl.ch/research/facilities/cmi/equipment/photolithography/acs200/>.
- [70] Mla150 machine. <https://www.epfl.ch/research/facilities/cmi/equipment/photolithography/heidelberg-instruments-mla150/>.
- [71] Veeco nexus ibe350 machine. <https://www.epfl.ch/research/facilities/cmi/equipment/etching/veeco-nexus-ibe350/>.

- [72] Tepla gigabatch machine. <https://www.epfl.ch/research/facilities/cmi/equipment/etching/tepla-gigabatch/>.
- [73] Vpg200 machine. <https://www.epfl.ch/research/facilities/cmi/equipment/photolithography/heidelberg-instruments-vpg200/>.
- [74] Spts aps machine. <https://www.epfl.ch/research/facilities/cmi/equipment/etching/spts-aps/>.
- [75] N.R. Rueger et al. Role of steady state fluorocarbon films in the etching of silicon dioxide using CHF_3 in an inductively coupled plasma reactor. *Journal of Vacuum Science Technology*, 15, 1998.
- [76] G. Levitin et al. Photoresist and etch residue removal. *Journal of The Electrochemical Society*, 153, 2006.
- [77] Evg150 machine. <https://www.epfl.ch/research/facilities/cmi/equipment/photolithography/evg-150-automatic-resist-processing-cluster/>.
- [78] Raith gdsii matlab toolbox. https://www.nanofab.ualberta.ca/2014/news/raith_gdsii-v-1-2-released/. Accessed : 2021.
- [79] H. Takei. Electrical resistivity of nb-ti superconductors. *Transactions of the Japan Institute of Metals*, 25, 1984.
- [80] T. Boutboul et al. Critical current density in superconducting nb-ti strands in the 100 mt to 11 t applied field range. *IEEE TRANSACTIONS ON APPLIED SUPERCONDUCTIVITY*, 16, 2006.

Abstract

Cryogenic systems such as superconducting coils magnets need distributed temperature sensing systems. However, most of the available thermometers require a significant number of cables, which creates inconveniences like parasitic heat conduction and refrigerant leakage, requirement for extensive feedthrough space. We propose in this thesis to investigate the potential of microwave kinetic inductance detectors (MKID) for cryogenic temperature sensing. After investigation of the superconductive and RF properties of MKIDs, we have optimized their design for this application. GHz-range resonators were made with 150 nm thin film NbTi on top of a sapphire substrate. Three fabrication methods (plasma etching, ion beam etching and lift-off) have been investigated to determine which one was the best suited to reach the lowest possible resolutions with optical lithography. It turned out that etching with fluorinated plasma allows the best resolutions on NbTi. A Matlab code assisted us in creating the layouts for many chips with different parameters and their properties were studied. We found a thin film NbTi resistivity of $8.8 \times 10^{-7} \Omega.m$ and a critical current density of 33 kA/mm^2 . The RF properties could not yet be investigated properly, but we understood how to make improvements on the electronic setup for the next RF measurements.

Les systèmes cryogéniques tels que les aimants à bobines supraconductrices ont besoin de systèmes de détection de température distribués. Cependant, la plupart des thermomètres disponibles nécessitent de nombreux câbles, ce qui crée des problèmes tels que des chemins de conduction thermique parasites et de fuite pour le réfrigérant, demande de la place pour les feedthroughs. Nous proposons dans cette thèse d'étudier le potentiel des détecteurs à inductance cinétique micro-onde (MKID) pour la thermométrie cryogénique. Après avoir étudié les propriétés supraconductrices et RF des MKID, nous avons optimisé leurs paramètres pour cette application. Des résonateurs dans la gamme des GHz ont été fabriqués avec un film mince de 150 nm de NbTi sur un substrat de saphir. Trois méthodes de fabrication (gravure plasma, gravure par faisceau d'ions et lift-off) ont été étudiées pour déterminer laquelle était la mieux adaptée pour atteindre les résolutions les plus basses possibles avec la lithographie optique. Il s'est avéré que la gravure par plasma fluoré permet les meilleures résolutions sur le NbTi. Un code Matlab nous a aidé à créer les layouts de nombreuses puces avec différents paramètres et leurs propriétés ont été étudiées. Nous avons trouvé une résistivité du NbTi en couche mince de $8,8 \times 10^{-7} \Omega.m$ et une densité de courant critique de 33 kA/mm^2 . Les propriétés RF n'ont pas pu être encore étudiées correctement, mais nous avons compris comment apporter des améliorations à la configuration électronique pour les prochaines mesures RF.

I sistemi criogenici come le bobine superconduttrici necessitano di sistemi di rilevamento della temperatura distribuiti. Tuttavia, la maggior parte dei termometri disponibili richiede molti cavi, il che crea problemi come la conduzione di calore parassita e perdite per il refrigerante, richiede spazio per i passanti. In questa tesi proponiamo di studiare il potenziale dei rivelatori di induttanza cinetica a microonde (MKID) per il rilevamento criogenico della temperatura. Dopo aver studiato le proprietà superconduttive e RF degli MKID, abbiamo ottimizzato il loro design per questa applicazione. I risonatori della gamma GHz sono stati realizzati con un film sottile di 150 nm NbTi su un substrato di zaffiro. Sono stati studiati tre metodi di fabbricazione (attacco al plasma, attacco a fascio ionico e sollevamento) per determinare quale fosse il più adatto a raggiungere le risoluzioni più basse possibili con la litografia ottica. Si è scoperto che l'incisione con plasma fluorurato consente le migliori risoluzioni su NbTi. Un codice Matlab ci ha aiutato a creare i layout per molti chip con parametri diversi e sono state studiate le loro proprietà. Abbiamo trovato una resistività NbTi a film sottile di $8.8 \times 10^{-7} \Omega.m$ e una densità di corrente critica di 33 kA/mm^2 . Le proprietà RF non potevano essere ancora studiate correttamente, ma abbiamo capito come apportare miglioramenti alla configurazione elettronica per le prossime misurazioni RF.